Title

A Stochastic Multiscale Model of Cardiac Thin Filament Activation Using Brownian-Langevin Dynamics.

Journal

Biophysical journal, 117(12)

ISSN

0006-3495

Authors

Aboelkassem, Yasser
McCabe, Kimberly J
Huber, Gary A
et al.

Publication Date

2019-12-01

DOI

10.1016/j.bpj.2019.08.003

Peer reviewed

A Stochastic Multiscale Model of Cardiac Thin Filament Activation using Brownian-Langevin Dynamics

Yasser Aboelkassem[a], Kimberly J. McCabe[a], Gary Huber[b], Michael Regnier[c], J.Andrew McCammon[b], Andrew D. McCulloch[a]

[a]*Department of Bioengineering, University of California San Diego, La Jolla, CA, USA*
[b]*Department of Chemistry and Biochemistry, University of California San Diego, La Jolla, CA, USA*
[c]*Department of Bioengineering, University of Washington, Seattle, WA, USA*

Abstract

We use Brownian-Langevin dynamics principles to derive a novel coarse-grained multiscale myofilament model that can describe the thin filament activation process during contraction. The model links atomistic molecular simulations of protein-protein interactions in the thin filament regulatory unit to sarcomere level activation dynamics. We first calculate the molecular interaction energy between tropomyosin and actin surface using Brownian dynamics simulations. This energy profile is then generalized to account for the observed tropomyosin transitions between its regulatory stable states. The generalized energy landscape then served as a basis for developing a filament-scale model using Langevin dynamics. This integrated analysis spanning molecular to thin filament scales is capable of tracking the events of the tropomyosin conformational changes as it moves over the actin surface. The tropomyosin-coil with flexible overlap regions between adjacent tropomyosins is represented in the model as a system of coupled stochastic ordinary differential equations. The proposed multiscale approach provides a more detailed molecular connection between tropomyosin dynamics, the trompomyosin-actin interaction energy landscape, and the generated force by the sarcomere.

Statement of Significance

Stochastic multiscale myofilament modeling can offer an enhanced mechanistic methodology to describe cardiac muscle contraction in both healthy and diseased subjects. In this study, we propose a coarse-graining multiscale (molecular-to-filament) model that can describe the activation process of the thin filament during sarcomere contraction. The model is based on Brownian dynamics at the molecular scale and Langevin dynamic stochastic processes at the filament scale. Our results provide for the first time a more detailed molecular connection between tropomyosin motions on the surface of actin filament and sarcomere force production.

1. Introduction

Sarcomeric missense mutations affect striated muscle contractility and can lead to various types of inherited cardiac diseases such as hypertrophic and dilated cardiomyopathies. Many of these mutations have been found to be distributed on tropomyosin (Tm) and actin residues and many are thought to modify the Tm-actin interaction energy landscape that regulates the Tm positioning and mobility on the surface of actin filaments. These mutations and post-translational modifications influence not only Tm dynamics, but affect myofilament Ca^{2+} sensitivity and alter cooperative interactions between actin, Tm, troponin-complex and myosin [1–8].

There are several Monte Carlo type myofilament models that have been used to analyse the functional effects of point mutations on sarcomere contractility [9, 10]. The exact molecular-to-filament mechanism by

which these alterations provide the trigger for disease progression and remodeling remains poorly understood. Because mutations can perturb the interaction energy landscape between Tm and actin, their effects cannot be explained by a filament-scale model that is either based on the mean-field approximation theory or relies purely on Markov type simulations. Therefore, more detailed modeling of myofilament biophysics will require a multi-scale approach to modeling thin filament activation that can link atomistic molecular simulations of protein-protein interactions in the thin filament regulatory unit to sarcomere level activation dynamics.

Brownian dynamics theory combined with Langevin dynamics can offer a coarse-grained mechanistic approach to bridging molecular-to-filament scales. This can be achieved by computing the interacting Tm-actin energy landscape from atomistic Brownian dynamics simulations and coupled with sarcomeric level activation dynamics. In fact, both theories have been used previously to explain the transition states guided by energy transformation in many molecular motors including but not limited to the myosin S1 attachment to the actin thin filament [11–18]. None of these models have directly addressed thin filament activation based on the dynamic motion of the Tm-coil on the surface of actin filament. Nevertheless, some of these models are still attractive and flexible enough that the cooperativity of the Tm coil/chain due to the nearest-neighbour interactions between the thin filament regulatory units (RUs) could be included explicitly in the system [9, 19–21].

Tm is a coiled-coil regulatory protein that binds head-to-tail to adjacent Tm molecules to form a continuous chain. When activated, this chain moves in the azimuthal direction (ϕ) over the actin filament surface. These dynamic motions of Tm are believed to play an important role in regulating muscle contraction [22–35]. Two different hypothetical mechanisms have been proposed to describe Tm motions on the actin surface. The sliding mechanism [36, 37] and the rolling mechanism [38, 39]. In either scenario (sliding or rolling), the Tm chain undergoes distinct movements to uncover the myosin-S1 binding sites located on the surface of the actin filament. These motions are characterized by three equilibrium positions, namely: the blocked position (B), closed position (C), and the open position (M) in the well-known three-state model of McKillop and Geeves [24]. Monte Carlo-based algorithms have been used to solve several mechanistic Markov state models of the intrinsic mechanisms by which Tm oscillates between the B-C-M states [36, 40–43]. Although these Markov-type models can be used to predict angular positions of the Tm-chain, their applicability in describing how Tm alternates between angular locations are limited. In addition, they cannot be used to track the intrinsic Tm dynamic motions between regulatory positions, which requires a stochastic multiscale molecular-to-filament approach.

In this study, we propose a coarse-graining (molecular-to-filament) multiscale model that can describe the activation process of the thin filament during sarcomere contraction. The model is based on Brownian dynamics at the molecular scale and Langevin dynamic stochastic processes at the filament scale. We begin by estimating a molecular-level energy landscape that regulates the Tm B-C-M conformational changes from Brownian dynamics simulations. We then used this energy landscape profile as a link between the atomistic model of Tm-actin interactions and a stochastic ordinary differential equation (SODE) model of cooperative thin filament activation dynamics. This approach demonstrates the capability of tracking spatiotemporal activation events of Tm oscillatory motions on the surface of the actin filament. It also provides for the first time a more detailed molecular connection between Tm motions on the surface of actin filament and sarcomere force production.

2. Materials and Methods

2.1. ***Brownian-Langevin Model Formulations***

We begin by deriving a model that can describe the azimuthal ϕ motions of the Tm molecules over the surface of the actin filament during activation. The model approximates a one-half sarcomere by N-coupled Brownian bodies, where each body indicates a Tm molecule that is associated with a single functional

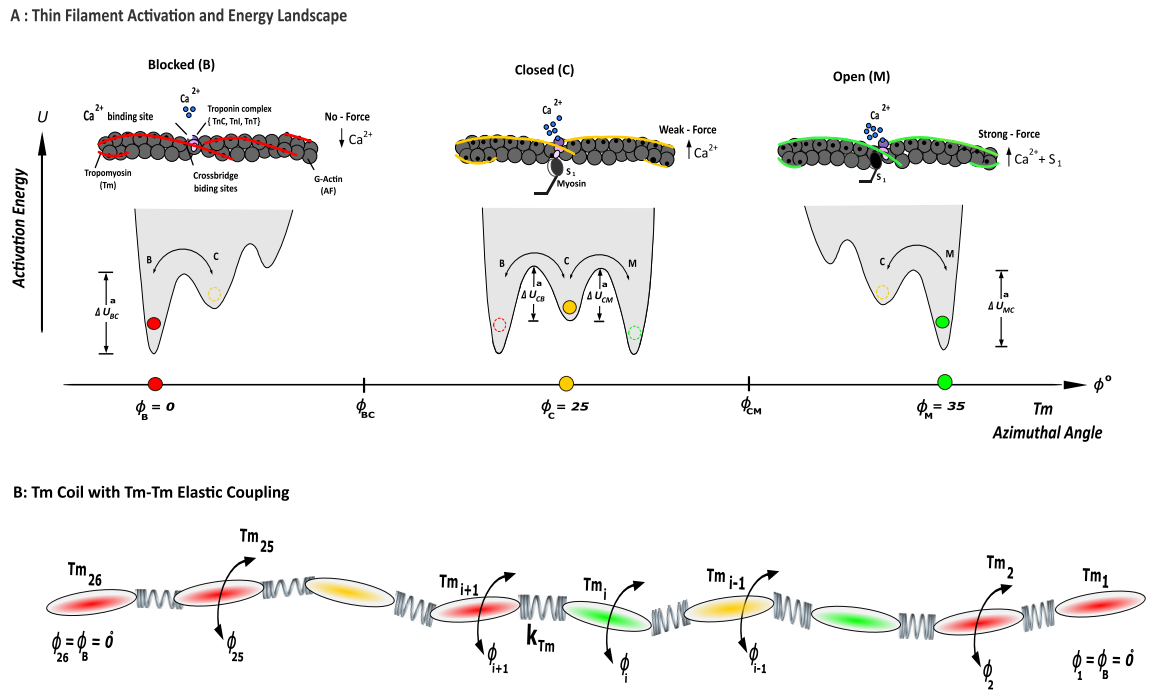

Figure 1: Langevin dynamics modeling components. Schematic diagrams that show the model activation energy and coupling strategy used to account for the Tm nearest-neighbor interactions. (A) The structure of myofilament main regulatory proteins and Tm B-C-M conformational positions and its dynamics as governed by a multi-well activation energy potential. (B) Representation of Tm chain as a coupled N-body oscillators to account for the nearest-neighbor interactions. An explicit expression of Tm-coil elastic distortion energy U_e is derived as a function of each Tm Brownian body i.e., for each RU.

RU. We use a total of N = 26 coupled RUs [9, 10, 19, 21]. Each RU is comprised of 7-actin monomers, troponin complex (Tn), Tm, and S1 subunit of myosin, Fig. 1. In the presence of thermal fluctuations, the equations that govern the motions of Tm molecules between B-C-M equilibrium states can be derived from the momentum balance along the reaction direction ϕ. Specifically, these equations can be derived by using the canonical form of Brownian dynamics of an overdamped system [44], which gives rise to the Langevin stochastic dynamics as,

$$\lambda\frac{d\phi_i}{dt} + \frac{d}{d\phi_i}\left[{U_i}^{a,BD}(\phi_i) + U^e(\phi_1, \phi_2, ...\phi_{25}, \phi_{26})\right] = \sqrt{2\lambda k_B T}\Gamma_i(t) \quad , i = 1:26 \tag{1}$$

subject to the following boundary and initial conditions:

$$\begin{aligned} &(i)\ \phi_1 = \phi_{26} = \phi_B, \quad \forall\, t \in (0, t_f) \\ &(ii)\ \phi_i = \phi_B, \qquad\quad when\ t = 0 \end{aligned} \tag{2}$$

where ϕ_i is the azimuthal angle of each Tm body, ϕ_B refers to the Tm angle at the B state, λ is the damping coefficient, k_B is the Boltzmann constant, T is the surrounding temperature in kelvin. ${U_i}^{a,BD}(\phi_i)$ is an activation potential energy which can be reconstructed using Brownian dynamic simulations [45]. This activation profile is then used to govern the regulatory motion of each Tm between its equilibrium positions. In addition to the activation energy, an expression for the Tm-coil elastic energy U^e is also required to account for the Tm coupling associated with each RU, also known as the nearest-neighbour interactions [19, 21]. In the above formulation, $U^e(\phi_i)$ represents the elastic distortion energy, which is used

to couple the Tm molecules using torsional springs K_{Tm}. An expression to the U^e will be derived in the next subsection. $\Gamma(t)$ is the total surrounding thermal noise that drives the Tm dynamics along the reaction coordinate. The thermal fluctuations are modeled using a Gaussian white noise distribution, which has a zero mean and satisfies the fluctuation-dissipation theorem,

$$\langle \Gamma(t) \rangle = 0 \qquad \& \qquad \langle \Gamma(t_1)\, \Gamma(t_2) \rangle = \delta(t_1 - t_2) \tag{3}$$

where δ is the Dirac delta function.

2.2. ***Nearest-Neighbour Interactions using Tm Elastic Distortion Energy, U^e***

In addition to the activation free energy ${U_i}^{a,BD}$, an expression for the Tm-coil elastic energy U^e is also required to account for the coupling among the Tm molecules associated with each RU, also known as the nearest-neighbour interactions [19, 21]. The nearest-neighbour interactions among RUs due to the overlap region between Tm molecules can be represented by deriving an elastic energy expression that accounts for the Tm distortion in the ϕ direction. We assume that the structural overlap between two Tm-Brownian bodies can be represented by a torsional spring [10]. This particular representation gives rise to a problem with 26-coupled oscillators with elastic energy expression depending on the number of RUs being used. This energy expression can be derived as follows:

$$U^e(\phi_i) = \frac{1}{2} k_{Tm} \begin{cases} 0 & if \quad i := 1 \\ 0 & := 2 \\ \left[(\phi_2 - \phi_1)^2 + (\phi_3 - \phi_2)^2\right] & := 3 \\ \left[(\phi_3 - \phi_2)^2 + (\phi_3 - \phi_2)^2 + (\phi_4 - \phi_3)^2\right] & := 4 \\ \left[(\phi_3 - \phi_2)^2 + (\phi_3 - \phi_2)^2 + (\phi_4 - \phi_3)^2 + (\phi_5 - \phi_4)^2\right] & := 5 \\ \vdots & \vdots \\ \vdots & \vdots \\ \left[{\phi_2}^2 + (\phi_3 - \phi_2)^2 + (\phi_4 - \phi_3)^2 + ... + (\phi_{24} - \phi_{23})^2 + (\phi_{25} - \phi_{24})^2 + {\phi_{25}}^2\right] & := 26 \end{cases} \tag{4}$$

Considering a total number of 26 RUs in one-half sarcomere, an expression of the elastic energy can be given as

$$U^e = \frac{1}{2} k_{Tm} \left[{\phi_2}^2 + (\phi_3 - \phi_2)^2 + (\phi_4 - \phi_3)^2 + ... + (\phi_{24} - \phi_{23})^2 + (\phi_{25} - \phi_{24})^2 + {\phi_{25}}^2\right] \tag{5}$$

In order to implement the model and track each Tm-body motion between B, C, and M states as a function of time, the derivative of equation (5) is required. In the following section, we outline this next step and describe the numerical details of the simulation.

2.3. ***Model Implementation and Numerical Algorithm***

A one-dimensional crystal composed of a total number of 26-RUs (i.e., 26 Tm-Brownian bodies) is considered. The angle of the first and last Tm molecules are used to specify the system boundary conditions, where both are set in the blocked state for all the simulation time. In other words, we set $\phi_1 = \phi_{26} = \phi_B = 0^\circ$ for all simulation times. The energetic barriers ($\Delta {U^a}_{BC}$, $\Delta {U^a}_{CB}$, $\Delta {U^a}_{CM}$ and $\Delta {U^a}_{MC}$) between the equilibrium B-C-M states have been found to strongly depend on the location of the critical roots (ϕ_{BC} and ϕ_{CM}) of activation free energy profile. This implies that the location of these critical roots implicitly represent the effects of free Ca^{2+} concentrations on the energy barriers. Once the critical roots become available at each Ca^{2+} concentration, the energy barriers are calculated, allowing for calculation of the transition rates (k_{BC}, k_{CB}, k_{CM}, k_{MC}) between the B-C-M states using the generic Eyring equation as follows:

$$k_{ij} = \frac{k_B T}{h} \exp\left(\frac{-\Delta {U^{a,BD}}_{ij}}{RT}\right), \quad i = \{B, C, C, M\}, j = \{C, B, M, C\} \,\&\, \; i \neq j \tag{6}$$

These transition rates are then used to estimate the maximum time step $\Delta t = \frac{1}{max(k_{ij})}$ required for a stable integration algorithm. h and R represent the Planck and the universal gas constants, respectively.

Once the activation free energy profile $U^{a,BD}$ (which be re-constructed using Brownian dynamics simulation) is available and we can establish an expression for the elastic energy U^e of the system under consideration. The coupled SODEs derived in equation (1) were integrated numerically using the Euler-Maruyama numerical method, which can be written as,

$$\phi_i(t_{n+1}) = \phi_i(t_n) - \frac{\Delta t}{\lambda}\frac{d}{d\phi_i}\left[U^{a,BD}(\phi_i(t_n)) + U^e(\phi_1(t_n), ..., \phi_{26}(t_n))\right] + \sqrt{\frac{2\Delta t k_B T}{\lambda}} W_i(t_n) \quad , i = 1:26 \quad (7)$$

where W_i is a random variable which is normally distributed with zero mean. Equation 7 can be rewritten in a non-compact form as

$$\begin{cases} \phi_1^{(n+1)} = \phi_1^{(n)} = 0 \\ \phi_2^{(n+1)} = \phi_2^{(n)} - A_1\left(\phi_2^5 - \alpha_1{\phi_2}^4 + \alpha_2{\phi_2}^3 - \alpha_3{\phi_2}^2 + \alpha_4\phi_2 - \alpha_5\right)^{(n)} - A_2\left(2\phi_2 - \phi_3\right)^{(n)} + A_3 W_2^{(n)} \\ \phi_3^{(n+1)} = \phi_3^{(n)} - A_1\left(\phi_3{}^5 - \alpha_1{\phi_3}^4 + \alpha_2{\phi_3}^3 - \alpha_3{\phi_3}^2 + \alpha_4\phi_3 - \alpha_5\right)^{(n)} - A_2\left(2\phi_3 - \phi_2 - \phi_4\right)^{(n)} + A_3 W_3^{(n)} \\ \vdots \\ \vdots \\ \phi_{25}^{(n+1)} = \phi_2^{(n)} - A_1\left(\phi_{25}^5 - \alpha_1{\phi_{25}}^4 + \alpha_2{\phi_{25}}^3 - \alpha_3{\phi_{25}}^2 + \alpha_4\phi_{25} - \alpha_5\right)^{(n)} - A_2\left(2\phi_{25} - \phi_{24}\right)^{(n)} + A_3 W_{25}^{(n)} \\ \phi_{26}(t_{n+1}) = \phi_{26}(t_n) = 0 \end{cases} \quad (8)$$

where, $A_1 = \frac{\Delta t U^{ref}}{\lambda}$, $A_2 = \frac{\Delta t k_{Tm}}{\lambda}$, and $A_3 = \sqrt{\frac{2\Delta t k_B T}{\lambda}}$. In all simulated cases, the system was assumed to be driven by thermal white noise at a constant damping level λ. However, it should be noted that this damping coefficient is an important parameter in the model and it could influence thin filament dynamics[46]. The initial conditions were chosen such that all Tm-bodies reside in the B-state. A summary of the k_B, h universal constants as well as simulation parameters is given in table 1. The value of U^{ref} is derived based on numerical stability requirement. The value of ϕCM is set at the midway point between the C and M states i.e. at $\phi CM = 30°$. We let ϕBC varies just between the B = 25 ° and C = 25°) states. More specifically, ϕBC is set to vary in a range between $\phi_{BC}^{min} = 1°$ and $\phi_{BC}^{max} = 24°$. Finally, the initial choice of K_{Tm} value is guided by the work in [47, 48].

For computational performance, the data parallel portions of the numerical simulations were implemented on NVIDIA-Tesla P4 8GB GPUs with data post-processing performed using MATLAB scripting and serial CPU code was implemented in C++. A copy of the code along with sample results are made available in the github repository: https://github.com/YasserAboelkassem/Tropomyosin-Dynamics. A single averaged force development response for a given Ca^{2+} concentration like those shown in Fig. 10 required about 0.1 s of wall clock time for typical parameter sets.

Time integration of the above equations (1) was then used to study all possible Tm dynamical responses when it moves over the actin surface during thin filament activation. The results from both the Brownian dynamics simulation and the Langevin dynamics simulations were used to show the temporal tracking of individual Tms and the induced developed contraction force as a function of the Ca^{2+} concentration are reported in detail in the following section.

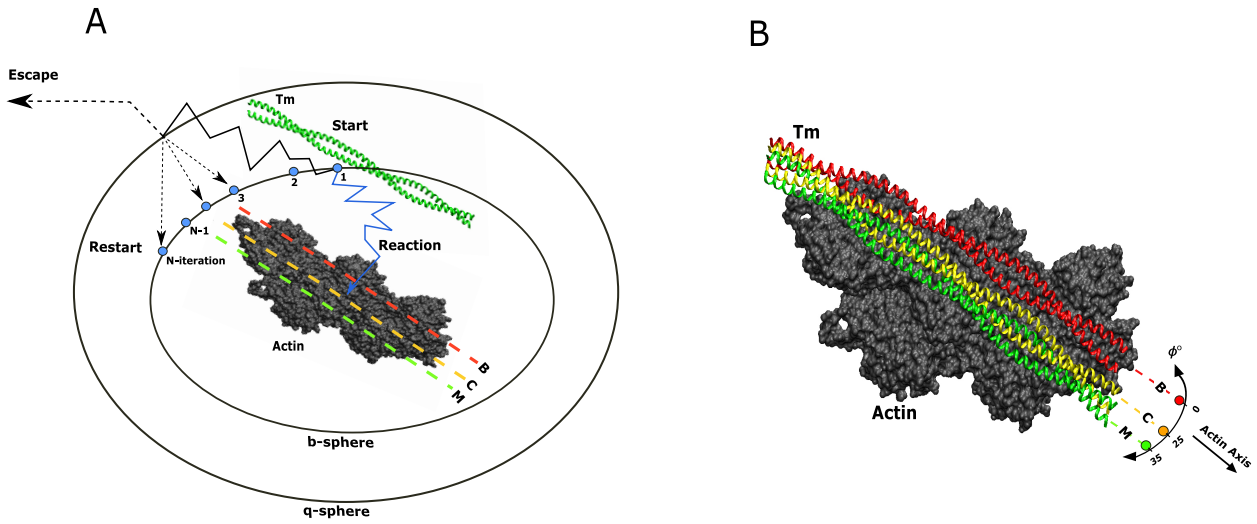

Figure 2: Brownian dynamics simulation setup to reconstruct the energy landscape profile of Tm azimuthal motions over actin surface. In panel A, we show our simulation setup with reaction (binding event) or escape of Tm-actin trajectories using the Browndye package developed by Huber and McCammon [45]. In panel B, we begin with PDB: 4A7F structure [37] positioned in the Tm open state (green ribbon) of approximately 35 degrees (using the blocked B state as the 0° reference). The atomic structure of Tm was then rotated about the axis of the actin thin filament at -2 ° decrements up to the blocked state at 0 degrees (red ribbon). The actin structure is shown in grey, with an intermediate Tm structure shown at 25 degrees of rotation, corresponding to the closed state (yellow ribbon).

3. Results

3.1. ***Brownian Dynamics Simulation***

Brownian dynamics simulations using the Browndye package [45] were used to calculate the second order association rate k_d $(1/M.s)$ between the Tm molecule and the actin filament as a function of the azimuthal angle ϕ. This is accomplished by generating between 1-2 million trajectories of interaction between a 272-residue Tm segment and a thin filament segment comprised of 5-actin monomers. The atomic structure used in the simulations was a crystallized actin-Tm-myosin complex in the rigor state (PDB: 4A7F), with myosins and ligands removed [37]. Using the Visual Molecular Dynamics (VMD) tools [49], the Tm segment is rotated (sliding only and without rolling) around the actin filament in the azimuthal direction at 2° increments up to 36° of rotation in order to cover the full range of Tm movements during thin filament activation. In other words, Tm was allowed only to slide without rolling on the actin surface during the course of simulations.

The initial configuration of the Tm-actin interactions that we used to run the Brownian dynamics simulations is shown in Figure 2A. Two spheres, namely the b-sphere and the q-sphere are centered around the actin filament. The radius of each sphere was set large enough so that the electric field was spherically symmetric. The center of the Tm starts on the b-sphere, and then undergoes Brownian motion steps until it either associates with the actin by satisfying distance constraints, or it reaches the q-sphere. If it reaches the q-sphere, an analytic solution to the diffusion equation is used to compute the probability of permanently escaping, or reaching the b-sphere again. A random number was used to determine its fate, and if it does not escape, it is placed back on the b-sphere, and the procedure is repeated until there is an association or an escape. This was repeated many times (labeled 1, 2, ..., N-Iteration) on Figure 2A), and the proportion of associations to escapes is used to compute the association rate constant.

The forces included in the model are steric repulsive force between individual atoms, the electrostatic interactions, and polar desolvation term. Before the simulation, the electrical field is computed around each molecule by treating the molecule and the solvent as continua and solving the Poisson-Boltzmann equation. During the simulation, the atomic charges on the Tm interact with the electric field on the actin. The present model does not include explicit hydrophobic interactions. Although they are important for absolute binding free energies, we assume here that the main determinant of differences in rate constant arises from the electrostatic interactions. More details about the Brownian dynamics simulations can be found in [45].

We begin our simulation with the rigor state (PDB 4A7F) structure positioned nearby the Tm open M state at about 35°. This atomic structure of the Tm was then rotated about the axis of the actin thin filament at $-2°$ decrements up to the blocked B state, which is defined at an angle of about 0°. The actin structure is shown in grey, with an intermediate Tm structure given at 25° of rotation, corresponding to the closed C state. In the the Browndye setup, both actin and Tm were treated as rigid bodies. The ribbon structures of the B-C-M states are rendered in red, yellow, and green respectively, as shown in Figure 2B.

The Tm and actin structures were converted to PQR format using pdb2pqr and the Amber force field package [50, 51]. The APBS solver was then used to generate electrostatic potential grids for the structures at 300K [52]. A permittivity value of 4 was set for the solute, and 78.5 for the solvent, with a solvent ion concentration of 0.15 M KCl corresponding to a Debye length of 7.86 Å. The electrostatic calculations for each actin-Tm configurations are then obtained. For instance, the electrostatic maps for both actin and Tm atomic structure in the open state is given in Figure 3. In particular, the electrostatic surface maps for both actin and Tm atomic structures are given in panel A and B respectively. The green dotted line represents the locus of the Tm location over the actin surface with landmark points 1, 2, and 3 given to highlight the interaction locations of both actin and Tm in the open M-state.

During the Brownian dynamics simulations, for each trajectory, the Tm fragment from PDB:4A7F was randomly spawned on a sphere a distance b (b-sphere) from the actin filament. The molecules move forward in time based on a combination of Brownian motion and intermolecular forces such as electrostatics, van der Waals interactions, and solvent effects. Elesctrostatic potentials are calculated out to the quadrupole level. The Tm fragment may move further away from the actin filament over time until it reaches an outer sphere at distance q (q-sphere), at which point the trajectory is considered to be an escape. Alternatively, the Tm fragment may move closer to within some prescribed reaction distance of the binding site on the actin filament, which is marked as an association event. The ratio of association to escape events is then used to derive a second-order association rate for the two molecules.

Figure 4A shows the calculated second-order association rate k_d for the Tm-actin complex as a function of the azimuthal angle ϕ at 5-different (12, 13.5, 15, 16.5, and 18 Å) reaction distances measured from the actin surface. An association event was considered to occur when 3-polar contact pairs were within the reaction distance set. These reaction distances were considered in order to compare the k_d-ϕ profile at multiple distances, and because there is no experimental data available to provide the exact rates of association between these molecules. Moreover, for each simulation, a set of contact atom pairs was generated to find likely hydrogen bonding pairs of atoms between the two molecules within 6 Å of each other. 1-2 million trajectories were performed for each Tm location. After completion of the trajectories, the ratio of association events to escape events was used to calculate a second order association rate. The results are then averaged and the standard errors of the mean are computed. The k_d-ϕ distribution has been found to exhibit multi extrema points that mimic the energetic barriers between the Tm transition states on the actin surface. The minima and maxima of the k_d distributions occurred at the same azimuthal location for all the tested reaction distances. The obtained rates are then used to reconstruct an approximate activation energy landscape ${U_i}^{a,BD}$ of the Tm-actin complex.

In Figure 4B, we show the reconstructed activation energy landscape of the Tm-actin complex as a function of the azimuthal angle (ϕ). The association rates computed from the Brownian dynamics simulations was

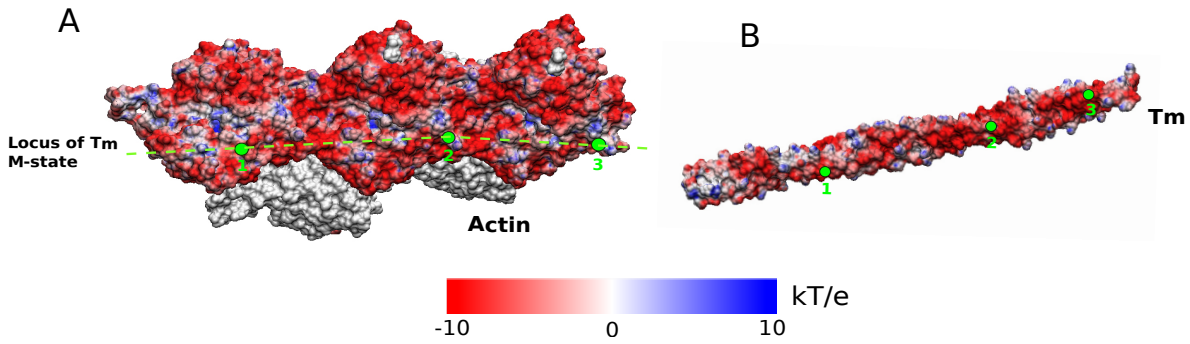

Figure 3: The electrostatic calculations that we initially used to run the Brownian dynamics simulations of the Tm motions on actin surface using the APBS package [52]. In panel A, we show the electrostatic surface map for the actin atomic structure. The surface coloring for the grey area is omitted for better visualization of the interacting side on the actin surface. In panel B, we show the electrostatic surface map for the Tm atomic structure. The green dotted line represents the locus of the Tm location over the actin surface with landmark points 1, 2, and 3 given to highlight the interaction locations of both actin and Tm in the open M-state corresponding to the original PDB crystal structure.

mapped to energy calculations using the Eyring formulation. This energy profile was accomplished by estimating high and low energy barriers for Tm as it rotates around the actin thin filament during sarcomere activation. Clearly, the energy-angle distribution demonstrates a multi-well topology. For instance, there are two clear minima that are located roughly at angles $\phi = 3$ and 26° respectively. These two angles represent the stable Tm locations on the actin surface and correspond to the B and C states. The maxima points of the energy profile represent the unstable points and mark the transition barriers required for the Tm to undergo conformational changes. It should be noted that, although the crystal structure complex around the 35° represents the rigor open state of Tm at full activation, this state is achieved through steric interactions with myosin-S1 heads in the physiological system. The computed energy profile does not show a clear minimum at this location. This is due to the lack of myosin-S1 head interactions considered in the Brownian dynamics simulations. However, the energy profile shows downward movement toward another stable point. The Brownian results of both the k_d and the ${U_i}^{a,BD}$ are then used to reconstruct activation energy profiles using piecewise, ϕ^4, and ϕ^6 potential functions to confirm the multi-well profile topology, as shown in Figure 4(B). These reconstructed potentials can then be used to integrate Langevin equations (1) and track the dynamical motions of Tm over the actin surface.

In Figure 5, we used the reconstructed piecewise potential to show sample results with a single realization of how each Tm is moving in time between both B and C states. This particular case is consistent with our Brownian dynamic simulation protocol where the myosin-S1 subunit is absent and hence the M state is not defined. The results have shown that as time progresses, Tms oscillate due to thermal noise until they gain enough energy to overcome the barrier $\Delta {U^a}_{BC}$, and move to the C state or back again to the B state. The sample results are shown only for two Tms on each side (i.e., ϕ_2, ϕ_3, ϕ_{24} and ϕ_{25})and for two Tms in the middle (i.e., ϕ_{12} and ϕ_{13}) of the half-length sarcomere.

In Figure 6, we show sample results with a single realization of how each Tm is moving in time between both B and C states, but using ϕ^4 potential. The results have shown that unlike the piecewise potential case, Tms tend to have more residence time in the B state and have difficulty overcoming the barrier $\Delta {U^a}_{BC}$ and move to the C state. Of course, it is hard to generalize this observation because we only show a single realization for each potential energy. Nevertheless, it should be noted that the Tm trajectory results generated by the double well potential can't be used to calculate the force-time development. These results will be used as a basis of a more generalized multi-well energy profile (e.g., ϕ^6) that accounts for the M state, which will allow for evaluation of the forces generated by the sarcomere.

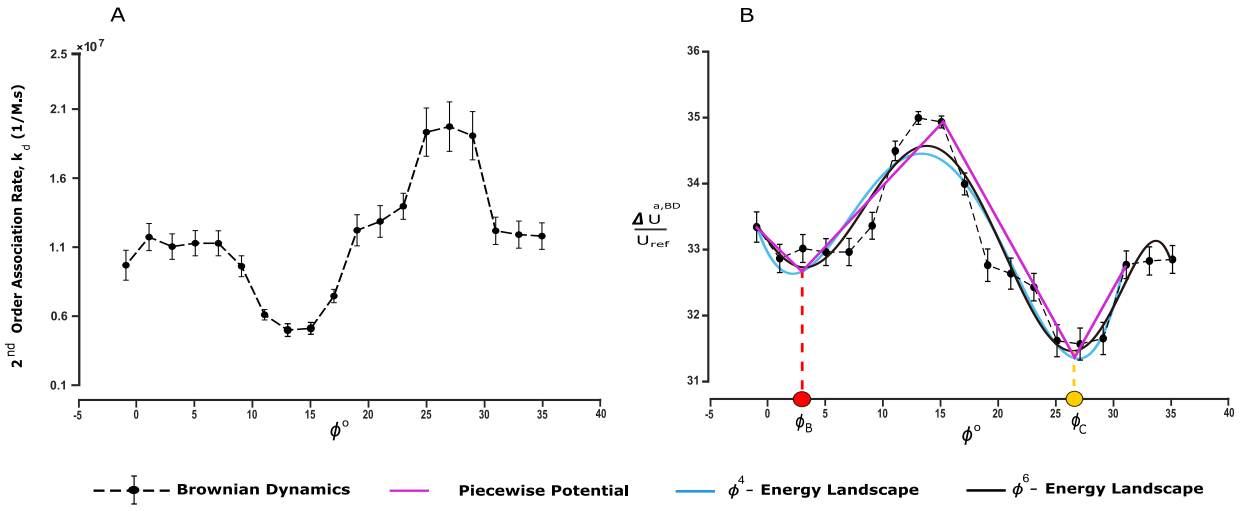

Figure 4: Estimating association rates and the multi-well energy landscape profile of Tm motion on the actin thin filament using Browndye [45]. In panel A, we show the averaged 2nd order association rates of Tm-actin complex (using results at 12, 13.5, 15, 16.5, and 18 Å reaction distances) as a function of the azimuthal positions of Tm on the actin filament. In panel B, we show the corresponding activation energy landscape profile calculated using Eyring formulation.The red and yellow circles refer to B and C states which are located at ϕ_B and ϕ_C, respectively. These two minimum values are predicated using the fitting of Brownian dynamics data.

3.2. ***A Generalized Multi-Well Energy Landscape as Guided by the Brownian Dynamics Simulation, $U^{a,BD}$***

We next use the results obtained from the Brownian dynamics simulations to derive a more generalized multi-well energy profile. This generalized activation free energy profile $U^{a,BD}(\phi)$ will be used in Langevin dynamics equation (1). The generalization of the energy potential is proposed such that it mimics the observed three-state (i.e., B-C-M) model [24]. This implies that the Tm azimuthal position ϕ on the surface of actin filament is governed by a potential function with a three-well (3-minima) topology. Each well corresponds to one of the B-C-M equilibrium positions as shown schematically in Figure 1. The location of these distinct equilibrium positions are taken from structural data [53, 54] which can be summarized as: (i) The blocked B state ($\phi = \phi_B = 0°$) refers to a situation where cytosolic Ca^{+2} ions are absent or very low, troponin T (TnT) is bound to Tm forming an interlocking troponin-tropomyosin complex, and troponin I(TnI) is bound to actin to hold the complex in place. (ii) The closed C state ($\phi = \phi_C = 25°$) exists when Ca^{+2} becomes available and binds to troponin C (TnC) which leads to a conformational change in TnC, allowing Tm to partially uncover the myosin binding site on the actin thin filament [55]. (iii) The open M state ($\phi = \phi_M = 35°$) is established when myosin binds to the thin filament, forms cross-bridges and undergoes the power stroke.

An expression of this multi-well activation energy profile can be mathematically formulated using a 6^{th}-order polynomial that has real and distinct roots as

$$U^a{}_i = U^{ref}\left[\frac{1}{6}{\phi_i}^6 - \frac{\alpha_1}{5}{\phi_i}^5 + \frac{\alpha_2}{4}{\phi_i}^4 - \frac{\alpha_3}{3}{\phi_i}^3 + \frac{\alpha_4}{2}{\phi_i}^2 - \alpha_5\phi_i\right] \quad , i = 1:26 \tag{9}$$

where,

$\alpha_1 = (T_1 + \phi_C)$

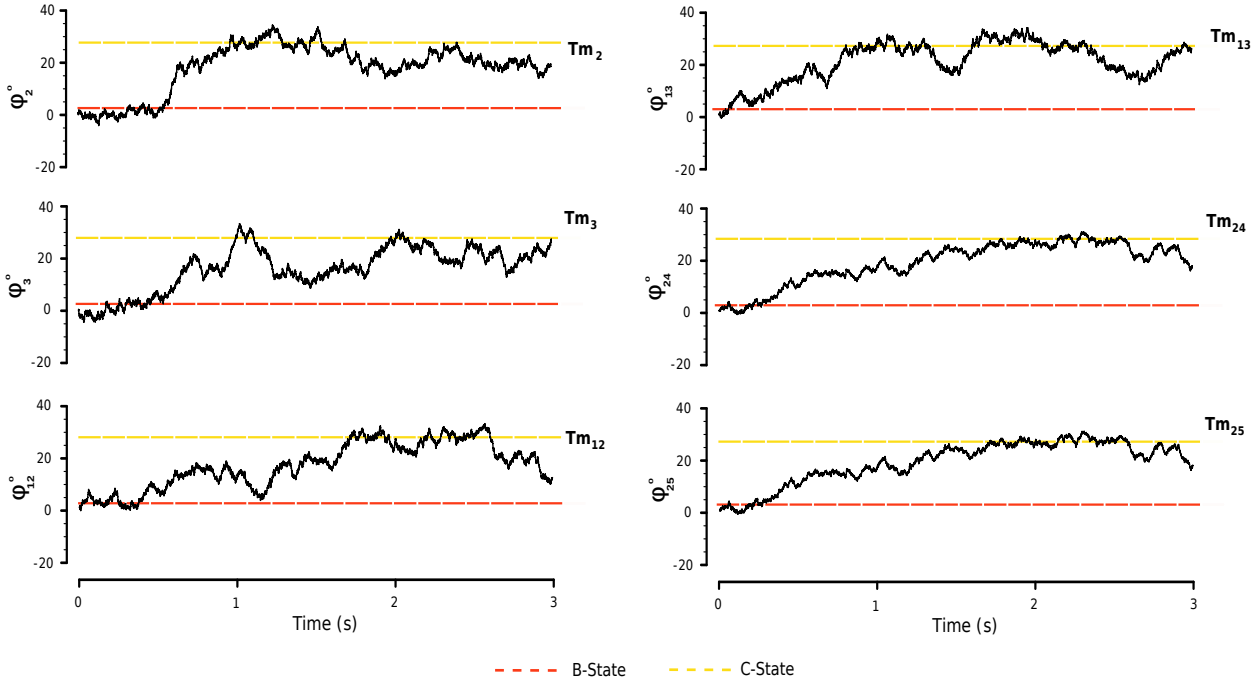

Figure 5: A single realization result showing the temporal tracking of a selection of 6-Tm molecules as they move between B and C equilibrium states using the a piecewise energy potential. This energy profile is reconstructed using the the Brownian dynamic results as shown in Figure 4. In this simulation, $\phi_{BC} = 12.5$ °, and the SODEs are then solved numerically for 3 seconds. The red and yellow dotted lines refer to the B and C equilibrium states predicated by using a piecewise energy potential, respectively.

$$\alpha_2 = (T_2 + \phi_C T_1)$$
$$\alpha_3 = (T_3 + \phi_C T_2)$$
$$\alpha_4 = (T_4 + \phi_C T_3)$$
$$\alpha_5 = (\phi_C T_4)$$
$$T_1 = (\phi_{CM} + \phi_{BC} + \phi_B + \phi_M)$$
$$T_2 = (\phi_{CM}\phi_{BC}) + (\phi_{CM} + \phi_{BC})(\phi_B + \phi_M) + (\phi_B\phi_M)$$
$$T_3 = (\phi_{CM}\phi_{BC})(\phi_B + \phi_M) + (\phi_B\phi_M)(\phi_{CM} + \phi_{BC})$$
$$T_4 = (\phi_{CM}\phi_{BC}\phi_B\phi_M)$$

The constant value of the reference energy U^{ref} is chosen to fulfill the numerical stability requirement of the Euler-Maruyama method, see Table 1. Moreover, it should be noted that the superscript "BD" in the energy term $U^{a,BD}(\phi)$ has been dropped for clarity. The above coefficients represent arbitrary parameters that depend only on the ϕ_{BC} and ϕ_{CM} critical roots of the free energy. These values control the shape, the activation barriers, and the critical (stable/unstable) points of the proposed energy landscape profile.

In Figure 7A, we show sample results of the generalized three-well potential (i.e., ϕ^6) derived in equation 9. Moreover, we show the effect of moving the root ϕ_{BC} on the energetic barriers of the activation free energy profile. In order to do so, we kept the other root ϕ_{CM} pinned midway point between ϕ_C and ϕ_M, setting $\phi_{CM} = 30$ °. As ϕ_{BC} moves toward the B-state, i.e., ϕ_B, the energy barrier between the B-C states and $U^a{}_{BC}$ decreases. In other words, the probability of Tm transitioning from the B-state to the C-state becomes higher as ϕ_{BC} moves to the left toward the ϕ_B root.

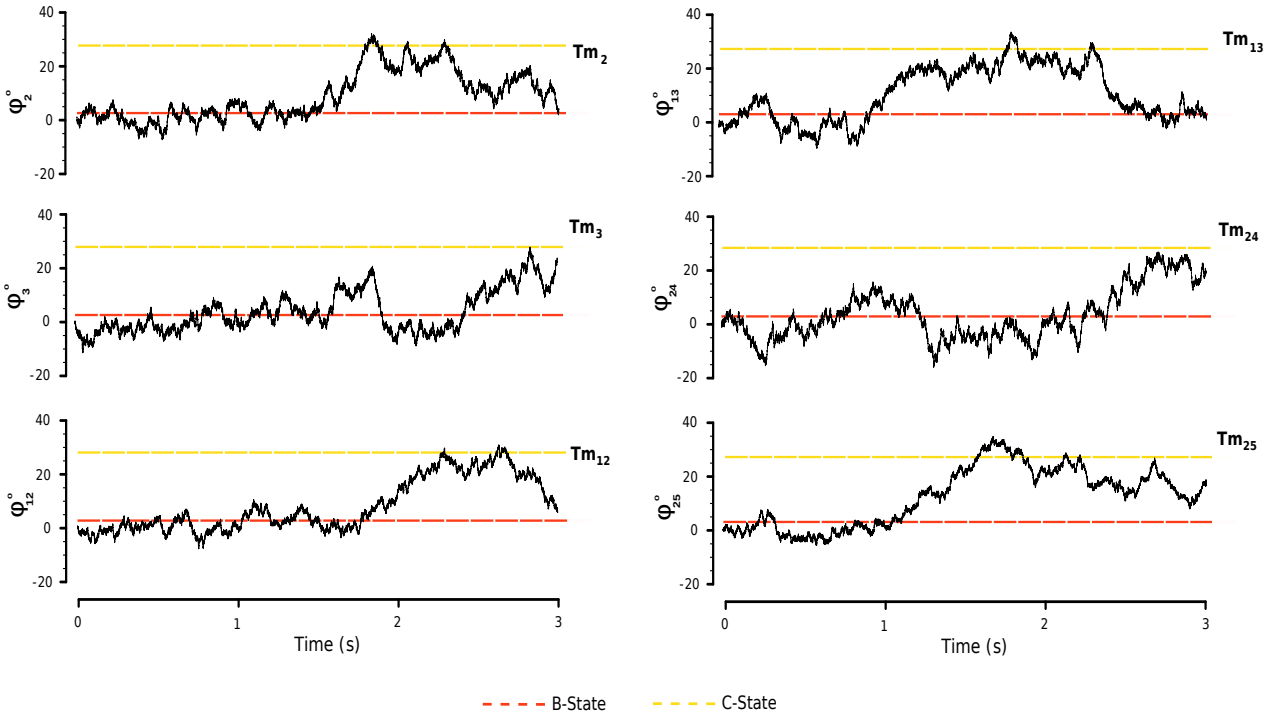

Figure 6: A single realization result showing the temporal tracking of a selection of 6-Tm molecules as they move between B and C equilibrium states using the ϕ^4-energy profile. This energy profile is reconstructed using the the Brownian dynamic results as shown in Figure 4. In this simulation, $\phi_{BC} = 12.5\ ^\circ$, and the SODEs are then solved numerically for 3 seconds. The red and yellow dotted lines refer to the B and C equilibrium states predicated by using a ϕ^4 energy potential, respectively.

This implicitly represents the process by which free Ca^{2+} ions bind to TnC and lower the energy required for Tm to transition from the B-state to the C-state. Therefore, we can hypothesize a connection between the free Ca^{2+} concentration, transition energetic barriers, and the location of ϕ_{BC}. This connection should satisfy certain observed criteria such as; (i) it should mimic the binding affinity of Ca^{2+} to TnC, which may be represented by Hill-type expression [56], and (ii) it should be consistent with the energy required in order for Tm to move from the B-state to the C-state. In equations (10-11), we propose the relationships between ϕ_{BC}, ϕ_{CM}, and Ca^{2+} as Hill-type sigmoidal functions in order to satisfy the criteria outlined above. These mathematical formulations are given to relate the critical root locations as a function of the Ca^{2+} concentrations:

$$\frac{\phi_{CM} - \phi_{CM}^{max}}{\phi_{CM}^{min} - \phi_{CM}^{max}} = \frac{1}{1 + \left(\frac{Ca^{50}_{\phi_{CM}}}{Ca^{2+}}\right)^{n_{\phi_{CM}}}} = \frac{1}{1 + 10^{n_{\phi_{CM}}\left(pCa - pCa^{50}_{\phi_{CM}}\right)}} \quad \forall\ \phi_{CM}^{min} > \phi_C\ \ \&\ \ \phi_{CM}^{max} < \phi_M \tag{10}$$

$$\frac{\phi_{BC} - \phi_{BC}^{max}}{\phi_{BC}^{min} - \phi_{BC}^{max}} = \frac{1}{1 + \left(\frac{Ca^{50}_{\phi_{BC}}}{Ca^{2+}}\right)^{n_{\phi_{BC}}}} = \frac{1}{1 + 10^{n_{\phi_{BC}}\left(pCa - pCa^{50}_{\phi_{BC}}\right)}} \quad \forall\ \phi_{BC}^{min} > \phi_B\ \ \&\ \ \phi_{BC}^{max} < \phi_C \tag{11}$$

In Figure 7B, we present the results by specifically implementing equation (11). These results clearly show a relationship between the free Ca^{2+} and the ϕ_{BC} root location. At high Ca^{2+} concentrations, the critical

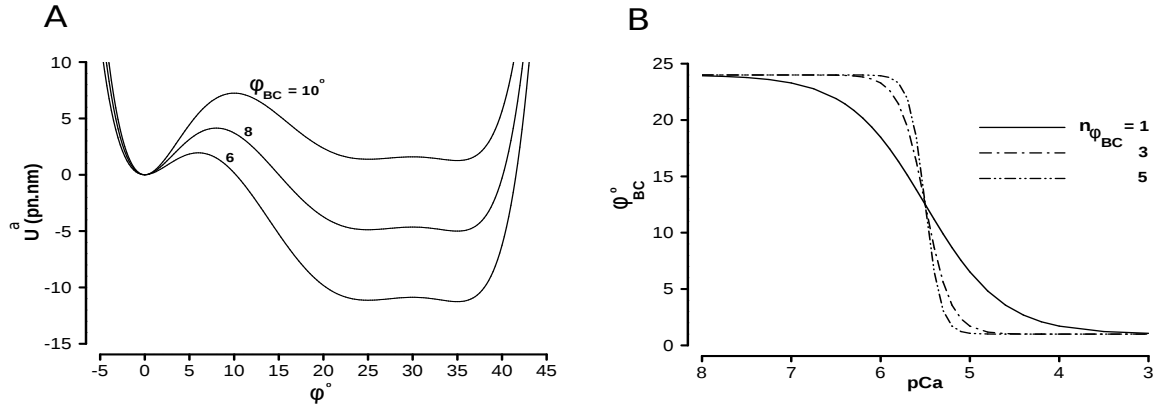

Figure 7: The activation free energy U^a profile as a function of Tm azimuthal direction ϕ and a Hill-type (sigmoid) relationship between the energy landscape root location ϕ_{BC} and pCa values. (A) The effects of varying ϕ_{BC} on the activation free energy while keeping $\phi_{CM} = 30\ ^\circ$ constant. (B) The effects of varying $n_{\phi BC}$ on the relationship between the location of the ϕ_{BC} and Ca^{2+} concentration, while keeping ${pCa^{50}}_{\phi_{BC}} = 5.5$ constant.

root ϕ_{BC} is located close to the blocked angle ϕ_B in order to lower ${\Delta U^a}_{BC}$. As the Ca^{2+} ions are depleted, the ϕ_{BC} root moves away from the blocked angle ϕ_B towards the closed angle ϕ_C, which in turn increases ${\Delta U^a}_{BC}$ and reduces the probability of Tm transitioning from the B-state to the C-state. The relationship is shown for different values of Hill coefficient $n_{\phi BC} = 1,\ 3,\ 5$, but at the same value of half-activation ${pCa^{50}}_{\phi_{BC}} = 5.5$. The two parameters, ${pCa^{50}}_{\phi_{BC}}$ and $n_{\phi BC}$, can therefore determine the location of ϕ_{BC} and alter the energy barrier for the B- to C-state transition.

Since the relationships between the free Ca^{2+} and the root angles of the activation free energy profile are now available, we can predict the effects of moving ϕ_{BC} and ϕ_{CM} on the energetic barriers between the B-C-M equilibrium states. In Figure 8, we show contour plots for all the energetic barriers (${\Delta U^a}_{BC}$, ${\Delta U^a}_{CB}$, ${\Delta U^a}_{CM}$, ${\Delta U^a}_{MC}$) as a function of both ϕ_{BC} and ϕ_{CM} root locations. These results show in particular the effect of varying both roots simultaneously on the energy profile morphology. For instance, the energy barrier between the B-C states ${U^a}_{BC}$ is shown in Figure 8 A. The range at which the Tm forward transition from the B-state to the C-state has the lowest energy barrier is $\phi_B < \phi_{BC} <\backsim 10^\circ$, irrespective of the location of the ϕ_{CM} root. This renders the backward energy barrier ${\Delta U^a}_{CB}$ for the reverse transition between C and B states to be the highest in the same range as shown in Figure 8 B. Similarly, the energetic barriers ${\Delta U^a}_{CM}$ and ${\Delta U^a}_{MC}$ that are associated with the Tm transitions between the C- and M-states are shown in Figure 7(C-D) respectively. The forward energetic barrier between C-M states ${\Delta U^a}_{CM}$ is the lowest in the range $\phi_C < \phi_{CM} <\backsim 29^\circ$ irrespective of the location of the ϕ_{BC} root, Figure 8 C. As expected, the backward energetic barrier ${\Delta U^a}_{MC}$ is highest in the same range as shown in Figure 8 D.

The results shown in Figure 8 are consistent with the fact that direct transitions between B and M states are prohibited. These results also suggest that there are only two independent parameters, namely ϕ_{BC} and ϕ_{CM}, that control the activation free energy morphology and hence the energetic barriers between the B-, C-, and M-states. These two parameters are hypothesized to be in direct connection with the free-Ca^{2+}, TnC, TnI-Tm interactions which shape the Tm activation energy landscape. It should be noted that the energetic barriers (${\Delta U^a}_{BC}$, ${\Delta U^a}_{CB}$, ${\Delta U^a}_{CM}$ and ${\Delta U^a}_{MC}$) between the equilibrium B-C-M states have been found to strongly depend on the location of the critical roots (ϕ_{BC} and ϕ_{CM}) of activation free energy profile. This implies that the location of these critical roots implicitly represent the effects of free Ca^{2+} concentrations on the energy barriers.

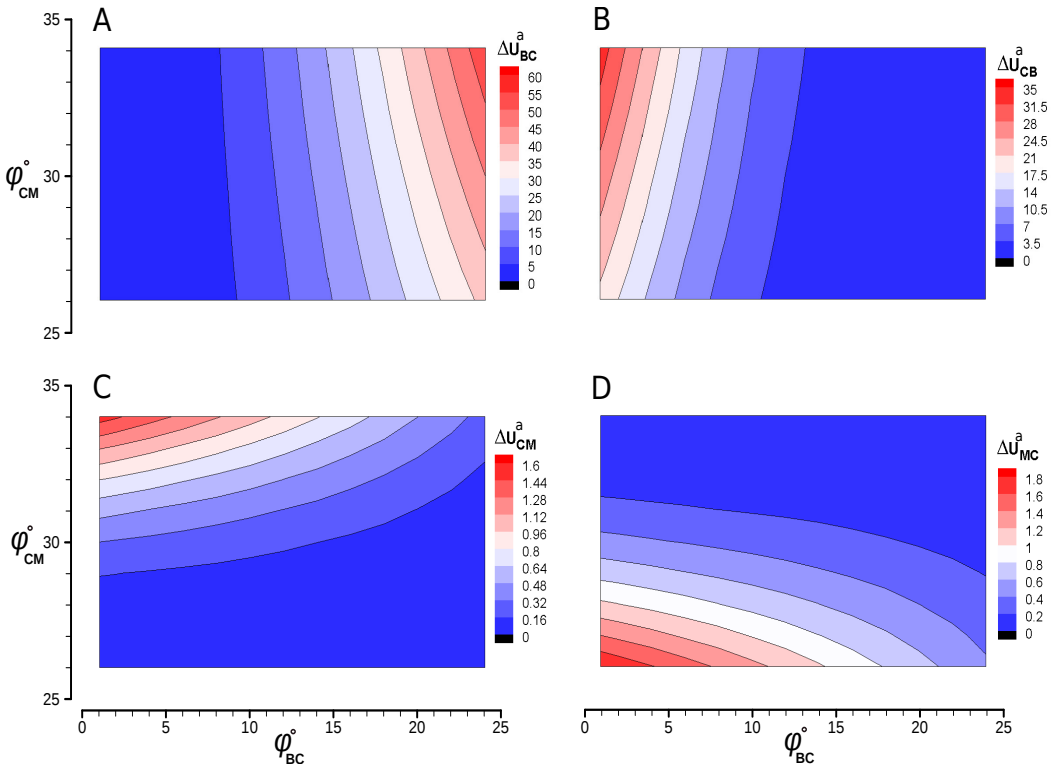

Figure 8: Contour plots of the activation free energy barriers between B-C-M as a function of both ϕ_{BC} and ϕ_{CM} roots. (A) Free energy barrier for Tm transition from B to C ($\Delta U^a{}_{BC}$) as a function of ϕ_{BC} and ϕ_{CM} root locations. (B) Free energy barrier for Tm transition from C to B ($\Delta U^a{}_{CB}$) as a function of ϕ_{BC} and ϕ_{CM} root locations ,(C) Free energy barrier for Tm transition from C to M ($\Delta U^a{}_{CM}$) as a function of ϕ_{BC} and ϕ_{CM} root locations,(D) Free energy barrier for Tm transition from M to C ($\Delta U^a{}_{MC}$) as a function of ϕ_{BC} and ϕ_{CM} root locations.

Table 1: Model constants and parameters

Parameter	λ	k_BT	h	U^{ref}	K_{Tm}	ϕ_{CM}	ϕ_{BC}^{min}	ϕ_{BC}^{max}
Units	(pN.nm.ns)	(pN.nm)	(pN.nm.ns)	(pN.nm)	(pN.nm/rad)	(rad)	(rad)	(rad)
Value	27π	4.1	$6.626\text{x}10^{-4}$	1000	10	$30\pi/180$	$1\pi/180$	$24\pi/180$

Now, having established a connection between the free Ca^{2+} and the location of the ϕ_{BC} root that controls the forward and backward transitions between B and C states, the stochastic system of equations 8 can be integrated in time at different Ca^{2+} concentrations.

3.3. ***Langevin Dynamics Simulations and the Sarcomeric Force-Ca^{2+} Sensitivity***

In order to calculate the force development at different levels of Ca^{2+} concentrations, a one-dimensional crystal composed of 26-RUs (i.e., 26 Tm-Brownian bodies) is considered. The angle of the first and last Tm molecules are used to specify the system boundary conditions, where both are set in the blocked state for all simulation times. In other words, we set $\phi_1 = \phi_{26} = \phi_B = 0^\circ$ for all simulation times.

In Figure 9, we show sample results with a single realization of how each Tm (associated with a single RU) moves in time between the B-C-M equilibrium positions using ϕ^6 potential. Unlike the results obtained from

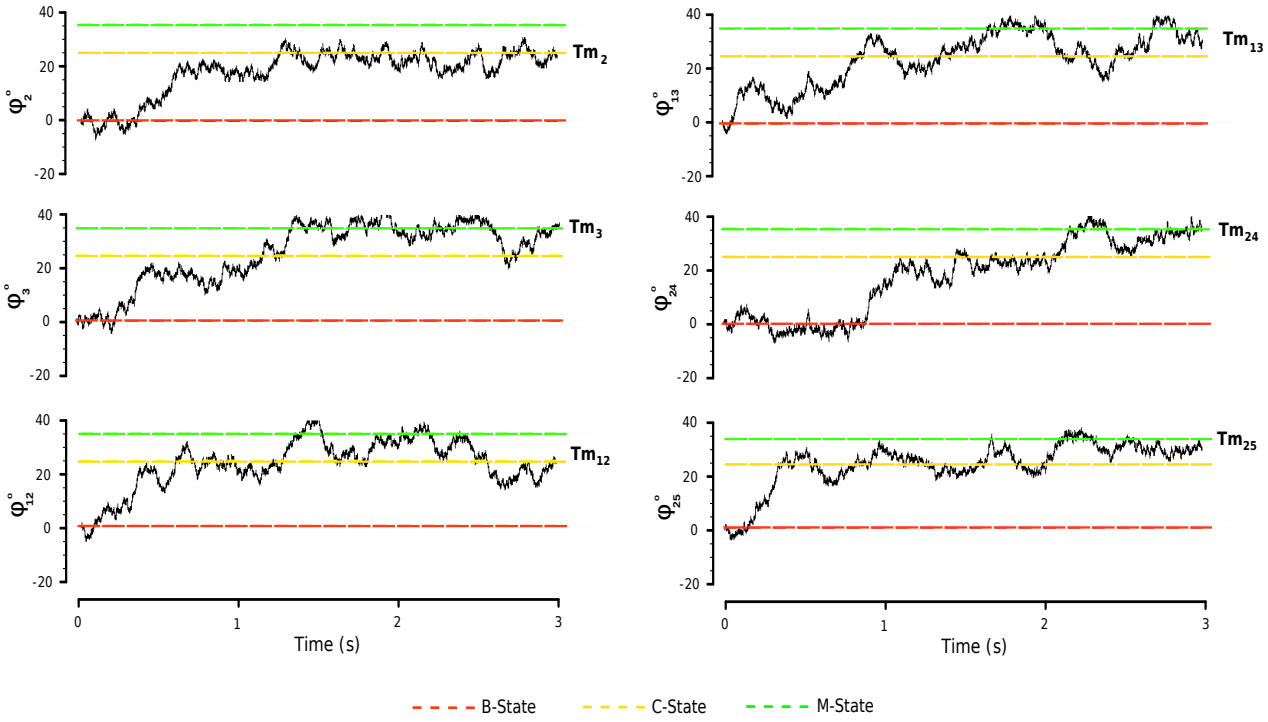

Figure 9: A single realization results showing the temporal tracking of a selection of 6 Tm molecules as they move between B-C-M equilibrium states, which are shown by the dotted lines. In this simulation, Ca^{2+} is held constant at pCa = 4.5, ${pCa^{50}}_{\phi_{BC}} = 5.5$ and $n_{\phi_{BC}} = 1$. The SODEs are then solved numerically for 3 seconds. We consider an RU to be in the B-state for $\phi = 0$ °, C-state for $\phi = 25$ °, and M-state for $\phi = 35$ °. The red, yellow and green dotted lines refer to the B-C-M state, respectively.

using the piecewise and ϕ^4 potentials which are shown in Figure 5 and Figure 6, respectively. In this case, as time progresses, Tms oscillate due to thermal noise until they gain enough energy to overcome the barriers ${\Delta U^a}_{BC}$ and ${\Delta U^a}_{CM}$, hence moving not only visiting the C state but also the M states. Once again, the sample results are shown only for two Tms on each side (i.e., ϕ_2, ϕ_3, ϕ_{24} and ϕ_{25})and for two Tms in the middle (i.e., ϕ_{12} and ϕ_{13}) of the half-length sarcomere. However, we have tracked the temporal evolution of the entire 26-Tms (i.e., 26 RUs) over 1024 repeated simulations in order to statistically evaluate the force producing events.

The force-producing events are scored when Tm is in the M-state, i.e., its torsional angle is at around 35° [53, 54]. That is because cross-bridges are not explicitly represented in the model, there is no consideration of cross-bridge kinetics. This effectively assumes that strong cross-bridges forms at any regulatory unit that achieves the M state and contribute a fixed amount of force. We then calculate the total relative force of the myofilament by adding up the number of RUs in the M-state at any given time and dividing this number by the total number of simulated RUs. Because of the stochasticity of the simulations, it is necessary to repeat the total simulation a large number of times and average the results. For our purposes, we repeated the SODEs solver 1024 times and averaged the results to develop smooth steady-state curves for each Ca^{2+} concentration.

In Figure 10, we demonstrate steady-state force development of the myofilament at different pCa values and at different values of $n_{\phi_{BC}}$. We vary the parameter $n_{\phi_{BC}} = 1$, 3, 5 as shown in panels A, B, and C, which governs the steepness of the cooperative relationship between Ca^{2+} and ϕ_{BC}. These time-force traces are

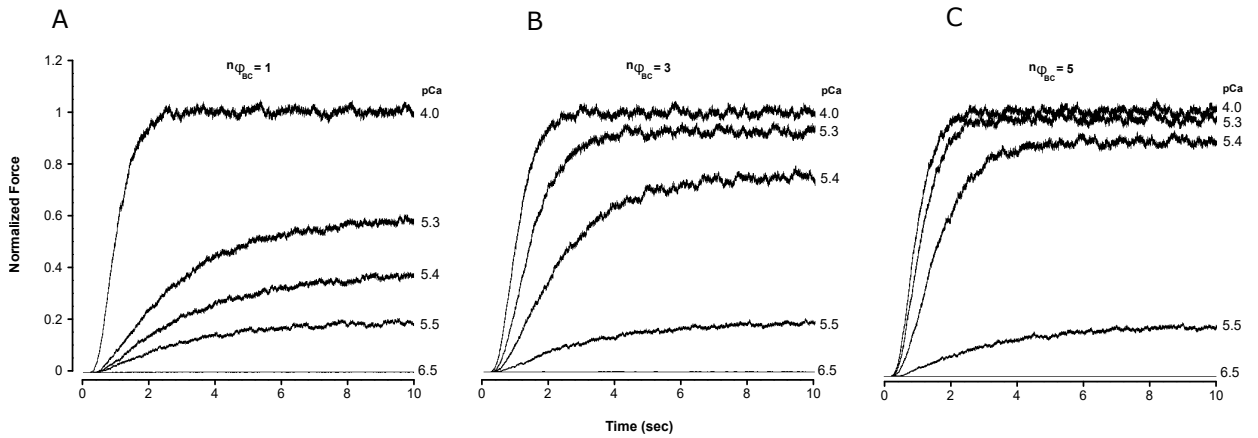

Figure 10: Time-force development at different levels of Ca^{2+} concentrations and for different values of $n_{\phi_{BC}} = 1, 3, 5$. These simulations were performed by setting $pCa^{50}{}_{\phi_{BC}} = 5.5$, Tm stiffness $K_{Tm} = 10$ and $\phi_{CM} = 30$ °. These results represent an average of 1024 realizations, where RUs in the M-state are considered to contribute equally to force.

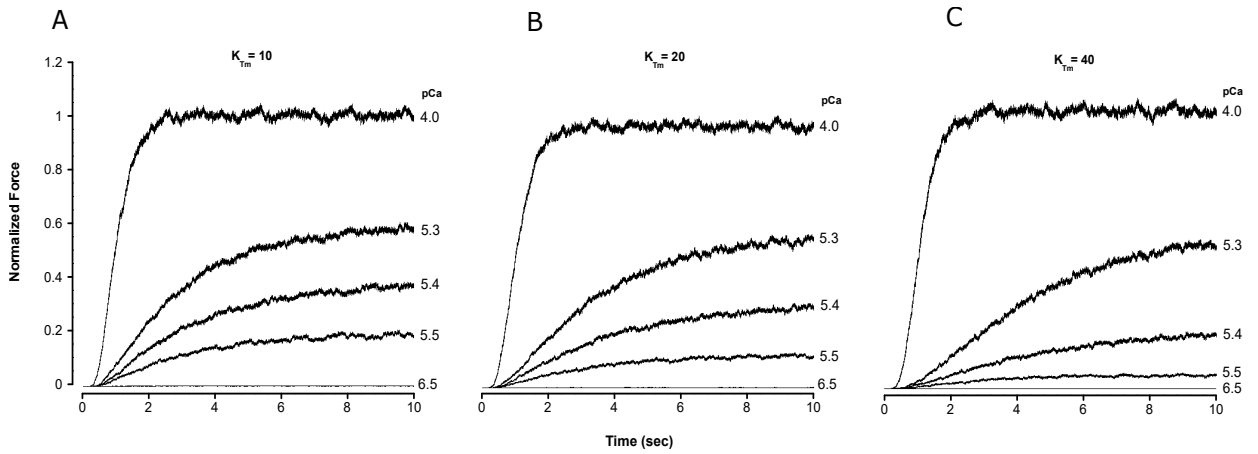

Figure 11: Time-force development at different levels of Ca^{2+} concentration and for different values of Tm stiffness $K_{Tm} = 10, 20, 40$ (pN.nm/rad). These simulations were performed by setting $n_{\phi_{BC}} = 1$, $pCa^{50}{}_{\phi_{BC}} = 5.5$ and $\phi_{CM} = 30$ °. These results represent an average of 1024 realizations, where RUs in the M-state are considered to contribute equally to force.

calculated by setting $pCa^{50}_{\phi_{BC}} = 5.5$ in equation (11) and at Tm stiffness $K_{Tm} = 10$ (pN.nm/rad). More results at different input value of $pCa^{50}_{\phi_{BC}} = 5.0, 5.5, 5.75$ are also obtained (not shown here) at $n_{\phi_{BC}} = 1$ and at $K_{Tm} = 10$ (pN.nm/rad). Similarly, the results showing the effects of varying the stiffness parameter $K_{Tm} = 10, 20, 40$ (pN.nm/rad) on the time-force development are also obtained and shown in Figure 11 where we set $n_{\phi_{BC}} = 1$ and $pCa^{50}_{\phi_{BC}} = 5.5$.

These results are further analyzed in order to obtain the steady-state force-pCa sensitivity and Hill parameters (n_H and pCa_{50}) in all studied cases, Figure 12. Clearly, adjusting the value of $n_{\phi_{BC}}$ has a large effect on the overall cooperativity of the steady-state force-pCa relationship where larger values of $n_{\phi_{BC}}$ correspond to higher cooperativity as shown in Figure 12A. This particular result suggests that when ϕ_{BC} is closer to ϕ_B (0°), the energy barrier governing the transition from B to C is smaller. In cases with higher $n_{\phi_{BC}}$, where

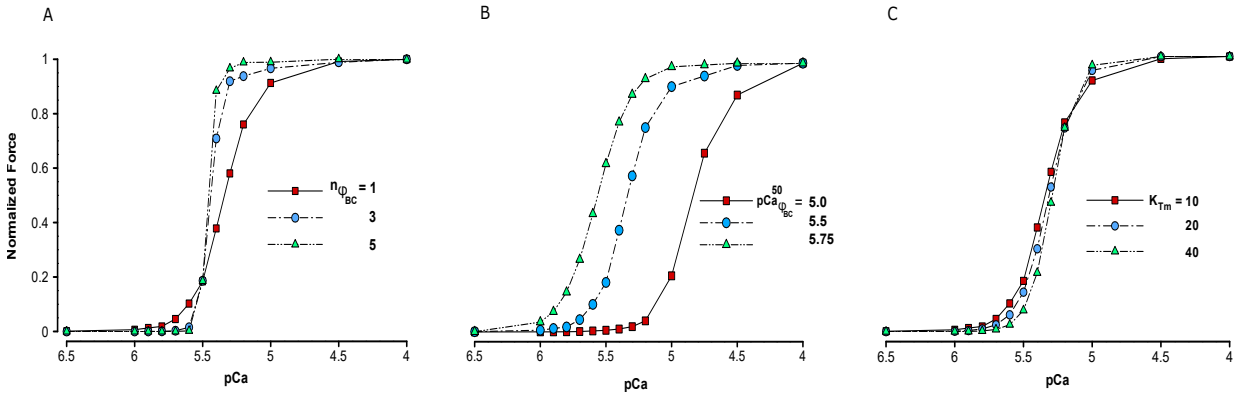

Figure 12: The force-Ca^{2+} sensitivity calculated by analyzing the time-force traces at different pCa values. These results are obtained at different values of $n_{\phi_{BC}}$, $pCa^{50}{}_{\phi_{BC}}$ and K_{Tm}, respectively. In panel A, we show results that are calculated by setting $pCa^{50}{}_{\phi_{BC}} = 5.5$ and at $K_{Tm} = 10$ (pN.nm/rad). In panel B, results are calculated by setting $pCa^{50}{}_{\phi_{BC}} = 5.5$ and $n_{\phi_{BC}} = 1$. In panel C, results are obtained by setting $n_{\phi_{BC}} = 1$ and $pCa^{50}{}_{\phi_{BC}} = 5.5$. All simulated cases are conducted by keeping $\phi_{CM} = 30\ ^\circ$ constant.

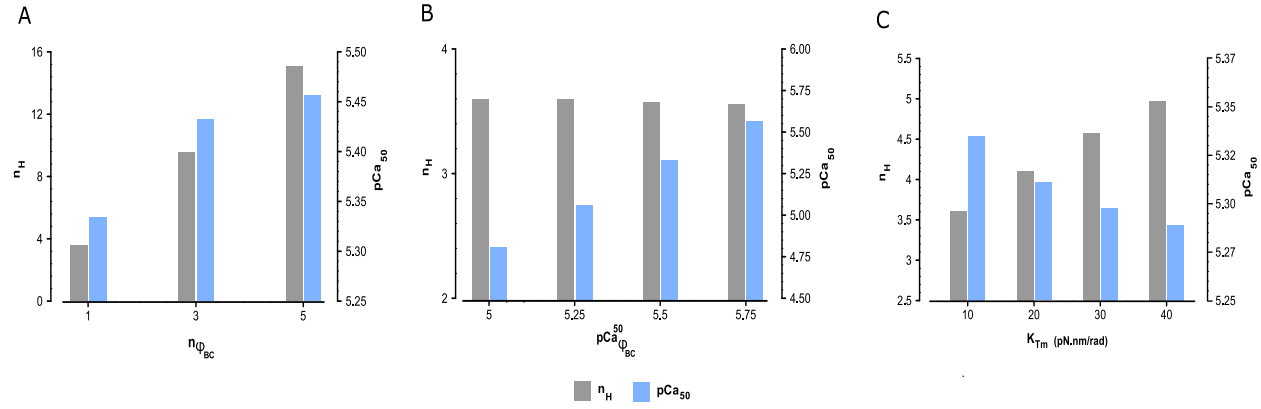

Figure 13: In panels A, B and C, we show the results of using Hill-best fitting characterization (i.e., n_H and pCa_{50}) for the force-Ca^{2+} results that were shown previously in Figure 7. In all panels, the fitted n_H and pCa_{50} values are shown on the left y-axis and on right y-axis.

ϕ_{BC} more quickly approaches ϕ_B as Ca^{2+} increases, we see a rapid force development. This is probably because the barrier from B to C becomes easier to overcome, which likely recruits more RUs to visit the M state downstream. In Figure 12B, we show the effects of $pCa^{50}_{\phi_{BC}}$ on the force-pCa sensitivity. The results show that increasing $pCa^{50}_{\phi_{BC}}$ can lead to significant changes in the pCa_{50} values without changing the Hill index.

One of the important parameters of the present model is Tm torsional stiffness, denoted by K_{Tm}. As described in the Methods section, the present study accounts for the Tm-Tm nearest-neighbour interactions and myofilament cooperativity, where the 26-RUs are coupled using an elastic energy expression U^e that depends on K_{Tm}. Additionally, previous studies have suggested that differences in the strength of Tm overlap due to disease or mutations can alter the cooperativity of the force-pCa curve [10, 57, 58]. Therefore, we have investigated the effects of K_{Tm} on the steady-state force-pCa solution. For instance, in Figure 12C, we

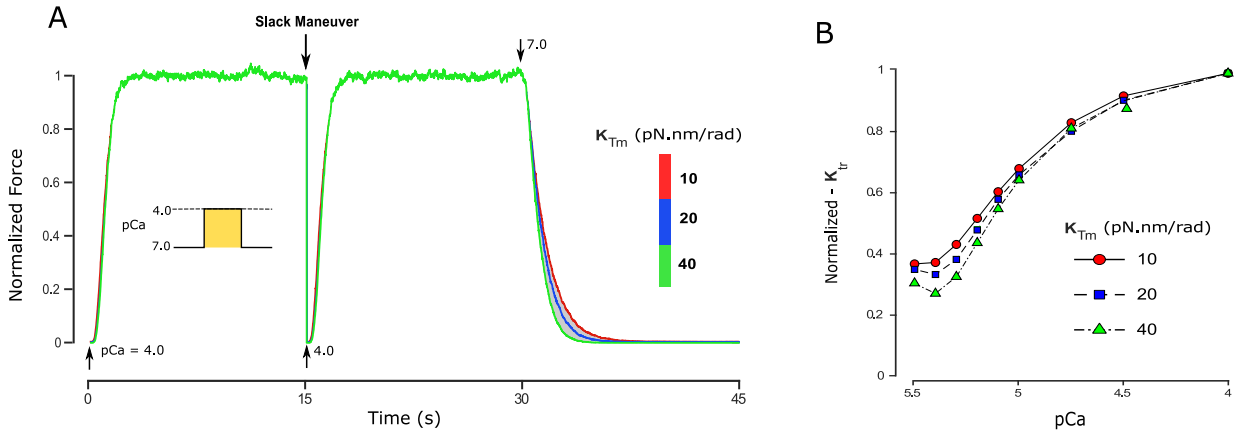

Figure 14: Model output for typical slack-restretch maneuver and rate of force redevelopment (K_{tr}) simulations. In panel A, we show the model prediction of the contractile force produced by the myofilaments during sudden exposure to Ca^{2+} and a slack/restretch maneuver mimicked by instantaneously removing all attached cross bridges. In panel B, we present the observed rate of force redevelopment K_{tr} as a function of pCa and at different values ofK_{Tm}.

demonstrate that altering the value of K_{Tm} indeed affects the cooperativity of the force-pCa relationship due to nearest-neighbour Tm interactions. We show that increasing K_{Tm} from 10 to 20 or 40 (pN.nm/rad) exaggerates the steepness of the force-pCa curve. The results show that increasing Tm stiffness decreases that apparent Ca^{2+}-sensitivity of steady-state isometric force and increases the slope.

The effects of varying $n_{\phi_{BC}}$, $pCa^{50}_{\phi_{BC}}$ and K_{Tm} on both Hill coefficient (n_H) and the half-maximal activation pCa_{50} of the force-pCa curves are given in Figure 13. The results suggest that as $n_{\phi_{BC}}$ increases from 1 to 3, pCa_{50} increases and then saturates while n_H appears to increase linearly, Figure 13A. These results imply that there is a strong connection between cooperativity of the ϕ_{BC} - Ca^{2+} relationship of equation(9) and the overall shape of the steady-state force-pCa curve. In other words, the topological changes in the activation energetic barriers as Ca^{2+} changes could have a strong influence on thin filament Ca^{2+} sensitivity. On the other hand, adjusting the value of $pCa^{50}_{\phi_{BC}}$ has a minor effect on the force-pCa cooperativity. We can see this in Figure 13B, where n_H appears to remain constant while pCa_{50} scales linearly with the $pCa^{50}_{\phi_{BC}}$ perturbations. Figure 13C outlines the effects of K_{Tm} on both pCa_{50} and n_H as well. There is a linearly increasing relationship between Tm-Tm overlap spring stiffness and Hill coefficient (n_H) of the curve. Conversely, there is a nonlinear decay relationship between K_{Tm} and pCa_{50}. In other words, increasing the torsional spring constant between Tm molecules leads to higher cooperativity of myofilament activation, but lower overall Ca^{2+} sensitivity.

In addition to the results that show the effects of K_{Tm} on F-pCa sensitivity and the associated cooperativity represented by pCa_{50} and n_H in Figures (12C-13C, we also show simulations to uncover the effects of Ktm on relaxation, activation, and redevelopment rates. Figure 14 shows the model results for a slack-restretch maneuver and rate of force redevelopment simulations at K_{Tm} = 10, 20, and 40 (pN.nm/rad). In Figure 14A, model predictions of the contractile force produced by the myofilaments during sudden exposure to Ca^{2+} are shown. In these records, Ca^{2+} was set to a higher value (pCa = 4.0) at time zero. After a period of rapid change (described by the activation rate constant), the force reached a steady-state level. A slack/restretch maneuver was then mimicked by instantaneously removing all attached cross bridges and observing the rate of force redevelopment K_{tr}. After the force reached again to a steady-state level, a sudden decrease in Ca^{2+} concentration was applied (pCa = 7.0). The force then declines and the rate of relaxation is observed. The results suggest that as K_{Tm} increases, a faster relaxation of developed force is achieved.

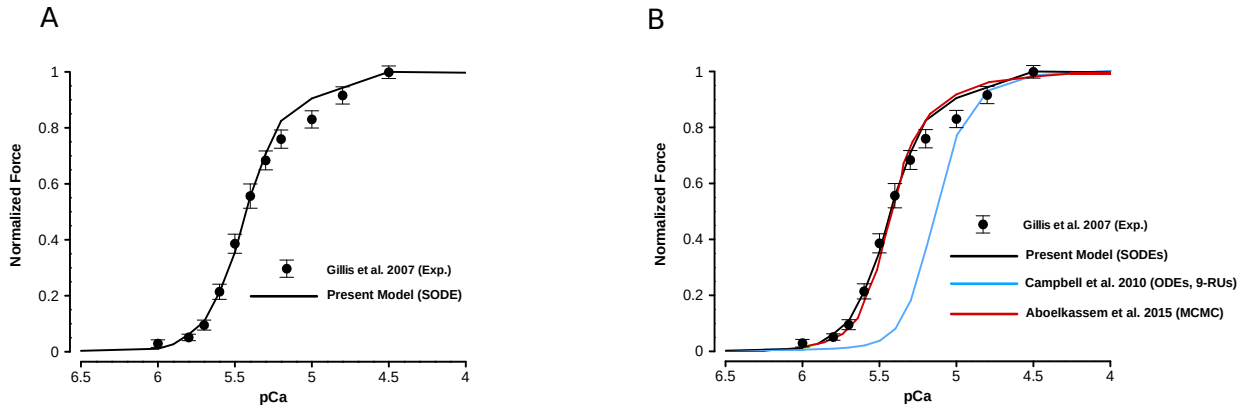

Figure 15: Model validation using force-pCa data from both experimental cardiac muscle preparation and previous computational models. In panel A, we show a comparison between our model and experimental data [59]. This result is obtained by adjusting the model parameters $n_{\phi_{BC}} = 1$, $pCa^{50}{}_{\phi_{BC}} = 5.55$, and $K_{Tm} = 1$ (pN.nm/rad). In panel B, we compare our model output with data generated numerically using other computational models [9, 21].

Table 2: Model type, number of parameters to be optimized, and accuracy represented by calculating the l_2-error norm when validated using experimental data set from [59].

Model	Type	Number of equations/states	Number of optimized parameters	$l^2 - norm = \sqrt{\sum_{i=1}^{N}(F_i^{Exp} - F_i^{Num})^2}$
Campbell et al 2010	ODEs	3^N eqs., N = # RUs	11	0.9004
Aboelkassem et al 2015	MCMC	6-states per 1-RU	12	0.1477
Present Model	SODEs	26 eqs.	3	0.1132

In Figure 14B, we present the observed rate of force redevelopment K_{tr} as a function of pCa and at different values of K_{Tm}. The results show that as K_{Tm} increases, a slower K_{tr} was observed for a fixed pCa value.

In Figure 15, we show the validation, accuracy, and performance of the current model when compared with both experimental data [59] and other nearest-neighbour computational myofilament models [9, 21]. For instance, in Figure 15A, a validation comparison between the current model and a force-pCa data from skinned cardiac muscle preparation is given. This simulation is obtained by adjusting the parameters $n_{\phi_{BC}} = 1$ and $pCa^{50}_{\phi_{BC}} = 5.55$ as well as the torsional stiffness $K_{Tm} = 1$ (pN.nm/rad) in order to best fit the experimental data. Moreover, in Figure 15B we show a comparison between the current Langevin-SODE model accuracy versus other ODE or Markov chain Monte Carlo (MCMC) based modeling approaches [9, 21]. The obtained results using similar/equivalent model parameters have shown that, unlike the ODE model, both the SODE and the (MCMC) simulations performed very well. A brief key summary between the three models is listed in Table 2.

4. Discussion

The main goal of the present coarse-grained myofilament modeling approach is to link the Tm-actin molecular energy landscape interactions to thin-filament scale activation using Brownian-Langevin dynamics. The

underlying idea of this study is based on fundamental theories explaining the molecular interactions of myofilament proteins during muscle contraction [60, 61], as well as on the mechanochemical coupling of the molecular motion to ATP hydrolysis [62, 63]. The use of Brownian-Langevin dynamics as a multiscale approach to describe myofilament activation can potentially move the field of cardiac mechanics toward more detailed atomistic models of subcellular function.

Brownian motion is fundamental to current atomistic-level investigations in both coarse-graining and all-atom molecular dynamics simulations which have been used to provide biophysical detail of many sarcomeric proteins [28, 64–75]. In particular, Brownian dynamics models of the actual molecules, built up from structural information at the molecular level, would constitute the next level toward the molecular end of the hierarchy of models [45, 76]. Such models might be able to provide the shape of the energy landscape along the reaction coordinate and the degree of coupling among adjacent Tm molecules [77]. Furthermore, recent work on coupling Brownian dynamics with more detailed molecular dynamics simulations could be used to explore the activation due to the Ca^{+2} ions [78, 79].

Previous computational models of thin filament activation have been useful for a variety of specific biological questions, but are often too computationally intensive or lack sufficient detail for certain applications. An example of a commonly used model of thin filament activation and cross-bridge cycling is given in [80]. Although this model allows for a quick and efficient solving a set of ODEs that describe the cross-bridge cycling, it ignores RU-RU interactions of the thin filament. A more spatially resolved ODE-based model was then developed to explicitly model Tm-Tm overlap and hence the RU-RU nearest-neighbour interactions [21]. Other models use MCMC processes to refine more thin filament details, but these simulations can become computationally expensive [9, 81, 82].

In this study, we derived a new SODE myofilament model based on the Brownian and Langevin dynamics. The Langevin component of the model has the capability to predict the spatiotemporal dynamics of Tm angular movements between the B-C-M equilibrium positions as a result of thermal fluctuations. The model is a natural extension of our previous myofilament studies, which use Markov type simulation and nonlinear dynamics to track Tm conformational changes and motions between the B-C-M states [9, 35]. The model allows us to accurately simulate steady-state force-pCa relationships using a number of equations exactly equal to the number of RUs (i.e., $N = 26$) without sacrificing spatial detail regarding Tm-Tm interactions. In terms of myofilament cooperativity, the mathematical description of the model includes two sources of cooperativity [83]. The first arises from Ca^{2+} binding to TnC which affects the energetic barrier between the B and C states. The second arises from the nearest-neighbour interactions (RU-RU cooperativity) which is represented by using an elastic distortion energy.

Brownian dynamics simulations were an essential component of this analysis. They reinforce the theory surrounding the multi-well energy landscape of Tm as it rotates about the actin thin filament. The results offer insight into the potential locations of high energy barrier points for the Tm-actin complex. The association rate distribution as a function of the azimuthal angle is used to derive a generic energy landscape in the absence of troponin and the myosin. The angles associated with the two local maxima in the association rate profile closely match the documented Tm positions in the B and C states, respectively. In these positions, strong electrostatic interactions between Tm and actin lead to minima in energy profile. The locations of the minima in the association rate landscape mark the energy barriers between both states. The open Tm state has been found to be energetically unfavorable without a bound myosin S1 head to push Tm to this extreme angle [84]. The 12.5° position should correspond to ϕ_{BC}, the angle at which a high energy barrier exists between the blocked and closed states.

It should be noted that, although the results of the Brownian dynamics show a multi-well energy profile, they don't demonstrate an energy minimum at the Tm open state for the following three reasons. Firstly, the myosin S1 is not included in the Brownian dynamics simulations and hence does not interact with the complex. We, however, hypothesize that bound myosin in the cross-bridge binding site on the actin thin

filament would greatly increase the energetic bias of the open state while minimizing association rates for all other positions. Secondly, we didn't consider the case of low cytosolic Ca^{2+}, in which the troponin complex sterically hinders Tm from moving out of the blocked state. In this case, one can assume the lowest energy well would exist at around zero degrees, with all other states becoming less favorable. Thirdly, our Brownian dynamics simulations considered only a portion of Tm which excludes the Tm-Tm overlap region, which makes it impossible to consider the effects of nearest-neighbor interactions on the energy landscape.

Recently, Tm dynamical movements on the surface of the actin filament were explained using an energy landscape perspective [84–88]. The results of these studies successfully predicted the azimuthal displacements of Tm (F-actin only) and its associated energy landscape potential, the latter shown to exhibit only a single energy minimum with a fairly broad well. Orzechowski and co-workers hypothesized that, when the rest (i.e., troponin and myosin) of the myofilament structure is considered, this single-well potential landscape will deform, allowing for multiple wells with various energy barriers to form [84]. These energy landscape results [84, 85, 87, 88] provide a useful platform that can be used to better understand the mechanistic role of Tm dynamics during muscle activation. However, the exact spatio-temporal mechanisms governing how the Tm-chain moves over the actin surface and which energy landscape it follows remain unresolved, hindering the complete understanding of Tm dynamics.

Herein, as demonstrated in equation (9), a more generic multi-well energy landscape (ϕ_6-potential) is derived based on the results obtained from the Brownian dynamics simulations. The proposed multi-well energy profile accounted for the fact that Tm must move between B-C-M equilibrium angles and considered variations in Ca^{2+} which impact the critical angles ϕ_{BC} and ϕ_{CM} that outline the energy barriers between the stable states. In the present results, the unstable location between the closed and open states ϕ_{CM} is kept fixed at the midway point between ϕ_C and ϕ_M. This led to the formation of a small energetic barrier ΔU_{CM} compared with ΔU_{BC}. However, the varying location of ϕ_{CM} could be used to control the myosin subunit S1 interactions, and hence the formation of crossbridges.

In summary, our coarse-graining modeling approach has shown the capability of tracking spatiotemporal activation events of the Tm motions on the surface of the actin filament. The model draws for the first time a more detailed molecular connection between Tm dynamical motions on the surface of actin filament and sarcomere force production. In addition, it produces sufficient cooperativity in the force-Ca^{2+} relationship and performs better than many of the current phenomenological myofilament models which were mostly derived based on mean-field approximation theory or Monte Carlo type simulations. The present Brownian-Langevin method is relatively simple and allows us to envision a unique energy profile that governs the activation of the thin filament via tracking Tm motions between B-C-M states during muscle contraction.

5. Model Limitations

One limitation of the current study is related to the lack of explicit handling of hydrophobic interactions during the Brownian dynamics simulations using Browndye software [45]. However, Lennard-Jones forces are calculated during trajectories which can be considered to approximate hydrophobic forces. Additionally, Browndye models both interacting molecules as rigid bodies rather than flexible chains. Therefore, the actual values of association rates are not physiologically relevant. For this reason, the exact choice of reaction distance was not relevant as all reaction distances tested had energy minima and maxima at the same azithumal locations. Moreover, the present Brownian dynamics simulation does not account for either twisting or unwinding effects. If these effects are included, we do expect changes in the energy profile topology and in the energetic barriers between the equilibrium states. A flexible chain version of the software is expected in the future, and further association studies should be performed at that time. If these effects are included, we do expect changes in the energy profile topology and in the energetic barriers between the equilibrium states. However, the main conclusion from modeling prospective will not altered.

Although our model accounts for Tm-Tm (i.e., RU-RU) interactions using torsional flexibility, other flexible missing components in the model might contribute to or impact the simulations. For instance, bending rigidity of Tm-Tm overlap region is not included in the model. It will be helpful to add bending elastic energy to account for the bending mode and mobility of Tm molecules, which will certainly affect the force-pCa relationship. Moreover, it has been demonstrated in prior studies that, to fully account for cooperativity at later stages of activation, one must account for crossbridge-crossbridge (XB-XB) and XB-RU cooperative effects as well [19, 82, 83]. This might explain the slow activation of the model. Therefore, further development of this model related to cooperativity will be required to strengthen prediction accuracy.

Finally, the model output focussed on analyzing the effects of parameters on the force-Ca^{2+} sensitivity and was quite limited regarding the validation of the model against experimental data. Further validation against experimental measurements is indeed required. For instance, comparing the model simulated twitches triggered by calcium transients against in-vitro measurements can be useful to test the model dynamic behavior. Additionally, fluorescence polarization data using bifunctional rhodamine attached specific residues on muscle proteins could be used to study orientations and/or dynamics of the labeled Tm proteins.

6. Conclusion

In this study, a coarse-graining mathematical model is derived to study Tm motions over the surface of actin filament during cardiac muscle contraction using hybrid Brownian-Langevin dynamics simulations. The model links the atomistic energy landscape of the Tm-actin interactions in the thin filament regulatory unit (RU) to sarcomere level activation dynamics. The proposed multiscale approach provides for the first time a more detailed molecular connection between Tm dynamic modes of motions, Tm-actin energy landscape, and force-Ca^{2+} sensitivity of the sarcomere. Thus, it is expected to be useful in better understanding Tm dynamics and its role in regulating the thin filament activation process when compared with Monte Carlo type simulations. Furthermore, this model is flexible enough that it can be developed further to investigate how, for example, Tm mutations modify the Tm-actin interaction energy landscape that regulates the Tm positioning and mobility on the surface of actin filaments. Therefore, the present Brownian-Langevin multiscale approach indeed may offer an enhanced mechanistic methodology to describe cardiac muscle contraction in both healthy and diseased subjects.

Author Contributions

YA derived the model theory; and YA, KJM, GH, and ADM designed and implemented the computational model; YA and KJM performed simulations; and YA, KJM, GH, MR, JAM, and ADM discussed the results and wrote the article.

Acknowledgement

This work was supported in part by National Institutes of Health awards No.R01 HL105242, R01 HL137100, U01 HL122199, U01 HL126273 to ADM and GM 31749 to GH and JAM. It was also supported in part by the National Biomedical Computation Resource 8P41GM103426 to ADM The authors acknowledge Dr. Joakim Sundnes from Simula Research Laboratory for his insightful discussions on the early draft of this manuscript.

References

[1] A. N. Chang, K. Harada, M. J. Ackerman, J. D. Potter, Functional consequences of hypertrophic and dilated cardiomyopathy-causing mutations in alpha-tropomyosin, J Biol Chem. 280 (2005) 34343–34349.

[2] M. C. Mathur, P. B. Chase, J. M. Chalovich, Several cardiomyopathy causing mutations on tropomyosin either destabilize the active state of actomyosin or alter the binding properties of tropomyosin, Biochem. Biophys. Res. Commun 406 (2011) 74–78.

[3] F. Bai, A. Weis, A. K. Takeda, P. B. Chase, M. Kawai, Enhanced active cross-bridges during diastole: Molecular pathogenesis of tropomyosin's hcm mutations, Biophys. J. 100 (2011) 1014–1023.
[4] F. Bai, P. B. Chase, Facilitated cross-bridge interactions with thin filaments by familial hypertrophic cardiomyopathy mutations in alpha tropomyosin, Biomed Biotechnol 435271 (2011) 1–12.
[5] J. Ochala, D. S. Gokhin, I. Penisson-Besnier, S. Quijano-Roy, N. Monnier, J. Lunardi, N. B. Romero, V. M. Fowler, Congenital myopathy-causing tropomyosin mutations induce thin filament dysfunction via distinct physiological mechanisms, Hum Mol Genet. 21 (2012) 4473–4485.
[6] C. Redwood, P. Robinson, Alpha-tropomyosin mutations in inherited cardiomyopathies, J. Muscle Res. Cell Motil. 34 (2013) 285–294.
[7] F. Bai, L. Wang, M. Kawai, A study of tropomyosin's role in cardiac function and disease using thin-filament reconstituted myocardium, J Muscle Res Cell Motil. 34 (2013) 295–310.
[8] G. P. Farman, M. J. Rynkiewicz, M. Orzechowski, W. L. J. R. Moore, Hcm and dcm cardiomyopathy-linked alpha-tropomyosin mutations influence off-state stability and crossbridge interaction on thin filament, Arch. Biochem. Biophys 647 (2018) 84–92.
[9] Y. Aboelkassem, J. A. Bonilla, . K. J. McCabe, S. Campbell, Contributions of ca^{2+}-independent thin filament activation to cardiac muscle function, Biophys J 109 (2015) 2101–2112.
[10] L. R. Sewanan, J. R. Moore, W. J. Lehman, S. G. Campbell, Predicting effects of tropomyosin mutations on cardiac muscle contraction through myofilament modeling, Front. Physiol. 7 (2016) 473.
[11] M. Meister, S. R.Caplan, H. C. Berg, Dynamics of a tightly coupled mechanism for flagellar rotation. bacterial motility, chemiosmotic coupling, protonmotive force, Biophys J 55 (1989) 905–914.
[12] R. D. Vale, F. Oosawa, Protein motors and maxwell's demons: does mechanochemical transduction involve a thermal ratchet?, Adv Biophys 26 (1990) 97–134.
[13] R. D. Astumian, Thermodynamics and kinetics of a brownian motor, Science 276 (1997) 917–922.
[14] R. F. Fox, Rectified brownian movement in molecular and cell biology, Phys Rev E 57 (1998) 2177–2203.
[15] T. R. Kelly, H. D. Silva, R. A. Silva, Unidirectional rotary motion in a molecular system, Nature 401 (1999) 150–152.
[16] D. Keller, C. Bustamante, The mechanochemistry of molecular motors, Biophys J 78 (2000) 541–556.
[17] R. Ait-Haddou, W. Herzog, Brownian ratchet models of molecular motors, Cell Biochem Biophys 38 (2003) 191–212.
[18] A. Vologodskii, Energy transformation in biological molecular motors, Phys Life Rev 3 (2006) 119–132.
[19] M. V. Razumova, A. E. Bukatina, K. B. Campbell, Different myofilament nearest-neighbor interactions have distinctive effects on contractile behavior, Biophys J 78 (2000) 3120–3137.
[20] M. Regnier, A. J. Rivera, C.-K. Wang, M. A. Bates, P. B. Chase, A. M. Gordon, Thin filament near-neighbour regulatory unit interactions affect rabbit skeletal muscle steady-state force-ca2+ relations, J. Physiol. 540 (2002) 485–497.
[21] S. G. Campbell, F. V. Lionetti...., A. D. McCulloch, Coupling of adjacent tropomyosins enhances cross-bridge-mediated cooperative activation in a markov model of the cardiac thin filament, Biophys J 98 (2010) 2254–2264.
[22] G. N. Phillips., J. P. Fillers, C. Cohen, Motions of tropomyosin. crystal as metaphor, Biophys J 32 (1980) 485–502.
[23] J. J. Earley, Simple harmonic motion of tropomyosin: proposed mechanism for length-dependent regulation of muscle active tension, Am J Physiol. 261 (1991) C1184–95.
[24] D. F. McKillop, M. A. Geeves, Regulation of the interaction between actin and myosin subfragment 1: Evidence for three states of the thin filament, Biophys. J. 65 (1993) 693–701.
[25] S. E. Hitchcock-DeGregori, Tropomyosin: function follows structure, Adv Exp Med Biol. 644 (2008) 60–72.
[26] P. Gunning, G. O'neill, E. Hardeman, Tropomyosin-based regulation of the actin cytoskeleton in time and space, Physiol Rev. 88 (2008) 1–35.
[27] C. Wang, L. M. Coluccio, New insights into the regulation of the actin cytoskeleton by tropomyosin, Int Rev Cell Mol Biol 281 (2010) 91 – 128.
[28] X. E. Li, K. Holmes, W. Lehman, H. Jung, S. Fischer, The shape and flexibility of tropomyosin coiled coils: Implications for actin filament assembly and regulation, J Mol Biol 395 (2010) 327–339.
[29] W. Zheng, B. Barua, S. E. Hitchcock-DeGregori, Probing the flexibility of tropomyosin and its binding to filamentous actin using molecular dynamics simulations, Biophys. J. 105 (2013) 1882–1892.
[30] M. El-Mezgueldi, Tropomyosin dynamics, J Muscle Res Cell Motil 35 (2014) 203–210.
[31] Y. Aboelkassem, N. Trayanova, Tropomyosin dynamics during cardiac thin filament activation as governed by a multi-well energy landscape, Biophys J 110 (2016) 524a.
[32] C. Risi, J. Eisner, B. Belknap, D. H. Heeley, H. D. White, G. F. Schröder, V. E. Galkin, Ca2+ -induced movement of tropomyosin on native cardiac thin filaments revealed by cryoelectron microscopy, PNAS 114 (2017) 6782–6787.
[33] Y. Aboelkassem, N. Trayanova, Tropomyosin fluctuations over a multi-well energy landscape: A brownian ratchet model of cardiac muscle contraction, Biophys J 112 (2017) 259a–260a.
[34] Y. Aboelkassem, K. J. McCabe, G. Huber, J. Sundnes, A. D. McCulloch, Turning the azimuthal motions of adjacent tropomyosins into a coupled n-body problem in a brownian model of cardiac thin filament activation, Biophys J 114 (2018) 502a–503a.
[35] Y. Aboelkassem, N. Trayanova, Tropomyosin dynamics during cardiac muscle contraction as governed by a multi-well energy landscape, Prog Biophys Mol Biol xx (2018) yy–zz.
[36] S. Mijailovich, O. Kayser-Herold, X. Li, H. Griffiths, M. Geeves, Cooperative regulation of myosin-s1 binding to actin filaments by a continuous flexible tm-tn chain, Eur Biophys J 41 (2012) 1015–1032.
[37] E. Behrmann, M. Muller, P. Penczek, H. Mannherz, D. Manstein, S. Raunser, Structure of the rigor actin-tropomyosin-myosin complex, Cell 150 (2) (2012) 327–338.
[38] C. Bacchiocchi, S. S. Lehrer, Ca^{2+}-induced movement of tropomyosin in skeletal muscle thin filaments observed by multi-

site fret, Biophys. J. 82 (2002) 1524–1536.
[39] M. F. L. Holthauzen, F. Correa, C. S. Farah, Ca^{2+}-induced rolling of tropomyosin in muscle thin filaments: the alpha- and beta-band hypothesis revisited., J Biol Chem 279 (2004) 15204–15213.
[40] D. Smith, R. Maytum, M. Geeves, Cooperative regulation of myosin-actin interactions by a continuous flexible chain i: Actin-tropomyosin systems, Biophys. J. 84 (2003) 3155–3167.
[41] D. Smith, M. Geeves, Cooperative regulation of myosin-actin interactions by a continuous flexible chain ii: Actin-tropomyosin-troponin and regulation by calcium, Biophys. J. 84 (2003) 3168–3180.
[42] M. A. Geeves, H. Griffiths, S. Mijailovich, D. A. Smith, Cooperative [ca^{2+}]-dependent regulation of the rate of myosin binding to actin: solution data and the tropomyosin chain model, Biophys. J. 100 (2011) 2679–2687.
[43] N. A. Metalnikova, A. K. Tsaturyan, A mechanistic model of ca regulation of thin filament in cardiac muscle, Biophys. J. 105 (2013) 941–950.
[44] D. L. Ermak, J. A. McCammon, Brownian dynamics with hydrodynamic interactions, J. Chem. Phys. 69 (1978) 1352–1360.
[45] G. A. Huber, J. A. McCammon, Browndye: a software package for brownian dynamics, Computer Physics Communications 181 (2010) 1896–1905.
[46] C. K. P. Loong, A. K. Takeda, M. A. Badar, J. S. Rogers, P. B. Chase, Slowed dynamics of thin filament regulatory units reduces ca2+-sensitivity of cardiac biomechanical function, Cell Molec Bioeng 6 (2013) 183–198.
[47] H. Kojima, A. Ishijima, T. Yanagida, Direct measurement of stiffness of single actin filaments with and without tropomyosin by in vitro nanomanipulation, PNAS 91 (1994) 12962–12966.
[48] C. K. P. Loong, H.-X. Zhou, P. B. Chase, Persistence length of human cardiac α-tropomyosin measured by single molecule direct probe microscopy, PLoS ONE 7 (2012) e39676.
[49] W. Humphrey, A. Dalke, K. Schulten, Vmd-visual molecular dynamics, J. Molec. Graphics 14 (1996) 33–38.
[50] T. Dolinsky, J. Nielsen, J. A. McCammon, N. Baker, Pdb2pqr: an automated pipeline for the setup, excution, and analysis of poisson-boltzmann electrostatics calculations, Nucleic Acids Research 32 (2004) W665–W667.
[51] D. Case, I. B.-S. ..., D. York, P. Kollman, Amber 2018, University of California, San Francisco.
[52] N. Baker, D. Sept, S. Joseph, M. Holst, J. A. McCammon, Electrostatics of nanosystems: application to microtubules and ribosome, Proc Natl Acad Sci, USA 98 (2001) 10037–10041.
[53] P. Vibert, R. Craig, W. Lehman, Steric-model for activation of muscle thin filaments, J Mol Biol 266 (1) (1997) 8–14.
[54] K. Poole, M. Lorenz, G. Evans, G. Rosenbaum, A. Pirani, R. Craig, L. Tobacman, W. Lehman, K. Holmes, A comparison of muscle thin filament models obtained from electron microscopy reconstructions and low-angle x-ray fibre diagrams from non-overlap muscle, J Struc Biol 155 (2006) 273–284.
[55] T. Kobayashi, R. Solaro, Calcium, thin filaments, and the integrative biology of cardiac contractility, Annu Rev Physiol 67 (2005) 39–67.
[56] J. D. Potter, J. Gergely, The calcium and magnesium binding sites on troponin and their role in the regulation of myofibrillar adenosine triphosphatase, J. Biolog. Chem. 250 (1975) 4628–4633.
[57] B. S. Pan, A. M. Gordon, Z. X. Luo, Removal of tropomyosin overlap modifies cooperative binding of myosin s-1 to reconstituted thin filaments of rabbit striated muscle, Journal of Biological Chemistry 264(15) (1989) 8495–8498.
[58] M. McConnell, L. T. Grinspan...., J. C. Tardiff, Clinically divergent mutation effects on the structure and function of the human cardiac tropomyosin overlap., Biochemistry 56 (26) (2017) 3403–3413.
[59] T. E. Gillis, D. A. Martyn, A. J. Rivera, M. Regnier, Investigation of thin filament near-neighbour regulatory unit interactions during force development in skinned cardiac and skeletal muscle, J. Physiol. 580 (2007) 561–576.
[60] A. F. Huxley, Muscle structure and theories of contraction, Prog Biophys Chem 7 (1957) 255–318.
[61] A. F. Huxley, R. Simmons, Proposed mechanism of force generation in striated muscle, Nature 233 (1971) 533–538.
[62] T. Mitsui, H. Ohshima, A self-induced translation model of myosin head motion in contracting muscle. i. force-velocity relation and energy liberation, J Muscle Res Cell Motil 9 (1988) 248–260.
[63] M. B. R. D. Astumian and, Mechanochemical coupling of the motion of molecular motors to atp hydrolysis, Biophys J 70 (1996) 637–653.
[64] P. Kekenes-Huskey, S. Lindert, J. McCammon, Molecular basis of calcium-sensitizing and desensitizing mutations of the human cardiac troponin c regulatory domain: A multi-scale simulation study, PLoS Comp Biol 8 (2012) e1002777.
[65] S. Lindert, P. Kekenes-Huskey, G. Huber, L. Pierce, J. McCammon, Dynamics and calcium association to the n-terminal regulatory domain of human cardiac troponin c: a multiscale computational study, J Phys Chem B 116 (2012) 8449–8459.
[66] J. Varguhese, Y. Li, Molecular dynamics and docking studies on cardiac troponin, C J Biomol Struct Dyn 29 (2011) 123–135.
[67] B. Ertz-Berger, H. He, C. Dowell, S. Factor, T. Haim, S. Nunez, S. Schwartz, J. Ingwall, J. Tardiff, Changes in the chemical and dynamic properties of cardiac troponin t cause discrete cardiomyopathies in transgenic mice, PNAS 102 (2005) 18219–18224.
[68] S. Dewan, K. McCabe, M. Regnier, A. McCulloch, S. Lindert, Molecular effects of ctnc dcm mutations on calcium sensitivity and myofilament activation-an integrated multiscale modeling study, J. Phys. Chem. B 120 (2016) 8264–8275.
[69] C. Loong, M. Badr, P. Chase, Tropomyosin flexural rigidity and single ca2+ regulatory unit dynamics: implications for cooperative regulation of cardiac muscle contraction and cardiomyocyte hypertrophy, Front. Physiol 3:80 (2012) 1–10.
[70] W. Lehman, G. Medlock, X. Li, W. Suphamungmee, A. Tu, A. S. et al, Phosphorylation of ser283 enhances the stiffness of the tropomyosin head-to-tail overlap domain, Arch. Biochem. Biophys 571 (2015) 10–15.
[71] X. Li, W. Suphamungmee, M. Janco, M. Geeves, S. Marston, S. F. et al, The flexibility of two tropomyosin mutants, d175n and e180g, that cause hypertrophic cardiomyopathy, Biochem. Biophys. Res. Commun 424 (2012) 493–496.
[72] W. Zheng, S. Hitchcock-DeGregori, B. Barua, Investigating the effects of tropomyosin mutations on its flexibility and interactions with filamentous actin using molecular dynamics simulation, J. Muscle Res. Cell Motil 37 (2016) 131–147.

[73] J. Varughese, J. Chalovich, Y. Li, Molecular dynamics studies on troponin (tni-tnt-tnc) complexes: insight into the regulation of muscle contraction, J. Biomol. Struct. Dyn 28 (2010) 159–174.
[74] J. Jayasundar, J. Xing, J. Robinson, H. Cheung, W. Dong, Molecular dynamics simulations of the cardiac troponin complex performed with fret distances as restraints, PLoS ONE 9.
[75] E. Manning, J. Tardiff, S. Schwartz, A model of calcium activation of the cardiac thin filament, Biochemistry 50 (2011) 7405–7413.
[76] T. Frembgen-Kesner, C. T. Andrews, S. Li, N. A. Ngo, S. A. Shubert, A. Jain, O. J. Olayiwola, M. R. Weishaar, A. H. Elcock, Parametrization of backbone flexibility in a coarse-grained force field for proteins (coffdrop) derived from all-atom explicit-solvent molecular dynamics simulations of all possible two-residue peptides, J. Chem. Theo. Comp. 11 (2015) 2341–2354.
[77] M. J. Rynkiewicz, T. Prum, S. Hollenberg, F. A. Kiani, P. M. Fagnant, S. B. Marston, K. M. Trybus, S. Fischer, J. R. Moore, W. Lehman, Tropomyosin must interact weakly with actin to effectively regulate thin filament function, Biophys. J. 113 (2017) 2444–2451.
[78] B. A. Luty, S. E. Amrani, J. A. McCammon, Simulation of the bimolecular reaction between superoxide and superoxide dismutase: Synthesis of the encounter and reaction steps, J.Am.Chem.Soc. 115 (1993) 11874–11877.
[79] L. W. Votapka, B. R.Jagger, A. L. Heyneman, R. E. Amaro, Seekr: Simulation enabled estimation of kinetic rates, a computational tool to estimate molecular kinetics and its application to trypsin-benzamidine binding, J. Phys. Chem. B 121 (2017) 3597–3606.
[80] J. Rice, F. Wang, D. Bers, P. D. Tombe, Approximate model of cooperative activation and crossbridge cycling in cardiac muscle using ordinary differential equations, Biophysical Journal 95(5) (2008) 2368–2390.
[81] P. B. Chase, J. Macpherson, T. Daniel, A spatially explicit nanomechanical model of the half-sarcomere: myofilament compliance affects ca 2+-activation, Annals of biomedical engineering 32(11) (2004) 1559–1568.
[82] B. C. W. Tanner, T. L. Daniel, M. Regnier, Filament compliance influences cooperative activation of thin filaments and the dynamics of force production in skeletal muscle, PLoS Comp Biol 8 (2012) e1002506.
[83] M. A. Geeves, S. S. Lehrer, Dynamics of the muscle thin filament regulatory switch: the size of the cooperative unit, Biophys. J. 67 (1994) 273–282.
[84] M. Orzechowski, J. R. Moore, S. Fischer, W. Lehman, Tropomyosin movement on f-actin during muscle activation explained by energy landscapes, Archives of Biochemistry and Biophysics 545 (2014) 63–68.
[85] X. Li, L. Tobacman, J. Mun, R. Craig, S. Fischer, W. Lehman, Tropomyosin position on f-actin revealed by em reconstruction and computational chemistry, Biophys. J. 100 (2011) 1005–1013.
[86] W. Lehman, A. Galinska-Rakoczy, V. Hatch, L. S. Tobacman, R. Craig, Structural basis for the activation of muscle contraction by troponin and tropomyosin, J. Mol. Biol 388 (2009) 673–681.
[87] W. Lehman, M. Orzechowski, X. Li, S. Fischer, S. Raunser, Gestalt-binding of tropomyosin on actin during thin filament activation, J Muscle Res Cell Motil 34 (2013) 155–163.
[88] M. Orzechowski, S. Fischer, J. R. Moore, W. Lehman, G. P. Farman, Energy landscapes reveal the myopathic effects of tropomyosin mutations, Archives of Biochemistry and Biophysics 564 (2014) 89–99.